Schizophrenia and autism associated mutations and disrupted m^{6}A signal by YTHDF1 cause defects in microtubule function and neurodevelopment

Rohini Roy[1,2,8], Xiangru Li[3,8], Shengqun Hou[1,2], Yoshie Fujiwara[1], Momoe Sukegawa[1,2], Wan-Ting Hong[1], Ikumi Oomoto[1,2], Hidenori Ito[4], Kandarp Joshi[1], Ruolin Fan[5], Koh-ichi Nagata[4], Kwok-on Lai[5], Dan Ohtan Wang[1,6,7]*

[1]Institute for Integrated Cell-Material Sciences (iCeMS), Kyoto University, Yoshida-Honmachi, Sakyo-ku, Kyoto, 606-8501, Japan

[2]Graduate School of Biostudies, Kyoto University, Yoshida-Honmachi, Sakyo-ku, Kyoto, 6068501, Japan

[3]School of Life Science and Biopharmaceutics, Shenyang Pharmaceutical University, Shenyang, Liaoning Province, China.

[4]Institute for developmental Research, Aichi Developmental Disability Center, Japan

[5]School of Biomedical Sciences, The University of Hong Kong,

[6]Wuya College of Innovation, Shenyang Pharmaceutical University, 110001, China

[7]The Keihanshin Consortium for Fostering the Next Generation of Global Leaders in Research (K-CONNEX), Yoshida-Honmachi, Sakyo-ku Kyoto-shi, Kyoto, 606-8501, Japan

[8]These authors contributed equally

To whom correspondence should be addressed.

Dan Ohtan Wang.

Tel: +81-75-753-9851;

Fax: +81-75-753-9820;

Email: dwang@icems.kyoto-u.ac.jp

Abstract

Building and maintaining neuronal networks and cognitive functions require mRNA localization and regulated protein synthesis in neurons. RNA modification *N*^{6}-methyl-adenosine (m^{6}A) has recently been shown in axonal and synaptically localized mRNAs whose local activity is required for axon growth, synaptogenesis, and neuronal plasticity. However, no cellular pathways engaging local epitranscriptomic modulation are known to underlie these post-mitotic neuronal functions. Now we report that cytoplasmic m^{6}A reader YTHDF1 is enriched in neurons and required for axonal, dendritic, and spine development. We show that m^{6}A and YTHDF1 are part of a microtubule plus-end associated RNA granule that contains extensive networks of mRNAs organized by autism risk gene adenomatous polyposis coli (APC). Disrupting m^{6}A signals by knocking down methyltransferase METTL14 or YTHDF1, or overexpressing autism or schizophrenia-associated missense mutations I311V or S399L in human METTL14, reduce expression of APC granule and tubulin, disrupt microtubule assembly and function. These results reveal a novel neuronal subcellular locus for epitranscriptomic regulation to promote post-mitotic neurodevelopment.

Introduction

Brain development and function are highly dependent on post-transcriptional gene regulatory mechanisms. These mechanisms arise from the highly complex needs of individual developing neurons with distinct morphological, electrophysiological, connection properties and activity histories, in addition to the elaborate geometry that demands compartmentalized gene expression[1]. A wide range of molecular and cellular pathways regulating RNA splicing, nuclear export, decay, editing, trafficking, and translation are involved in neuron polarization, migration, axon guidance, dendritic development, and synaptic plasticity[2–11]. In parallel, mounting evidence has linked dysregulated post-transcriptional regulation and resulting aberrant protein production to neurodevelopmental, neuropsychiatric, and neurodegenerative diseases[12–15].

Epitranscriptomics, a field concerning genetic deciphering based on the type- and site-specific RNA modifications, has recently emerged as a versatile and powerful post-transcriptional regulatory pathway in the central nervous system[16]. Today, more than 170 types of chemically modified nucleotides with varied structures and physicochemical properties are known to exist in nature[17]. Although the biological functions remain to be explored for most of them, characterization on some abundant RNA modifications have shown that they are strategically positioned to the evolutionarily conserved and functionally important sites of RNA molecules where they critically influence the function of the modified RNAs. In addition, cells have dedicated molecular machinery to deposit (write), remove (erase), and recognize (read) specific types of RNA modifications, rendering epitranscriptomic gene regulation dynamic, reversible, and tunable[16,18,19]. Among many modified nucleotides (e.g. inosine, 2'*O*-methylation,

5-methylcytosine), arguably the best characterized messenger RNA modification in the central nervous system is N^6-methyl-adenosine (m^6A), the most abundant internal RNA modification in mammals which decorates up to half of the entire poly(A) transcriptome in the brain tissue[20]. Our advanced understanding of m^6A can be attributed to the identifications of its "writer" complex (containing METTL3, METTL14, WTAP, and other subunits of the methyltransferase), "erasers" (FTO and ALKBH5), and "readers" (YTH family proteins, hnRNPC, hnRNPG, IGF2BPs, eIF3, etc.), that manipulations of these factors in cells or in the whole organism have helped reveal the detailed functions of this modification[20]. m^6A has been shown to play critically important roles in cortical neurogenesis[21,22], axon guidance[23,24], circadian rhythm[25], learning and memory[26–28], reward[29], addiction[30], stress[31], and spinal injury[32], etc. The functional significance of m^6A highlights the importance of spatiotemporal aspects of gene regulation in the central nervous system, as m^6A does not render amino acid changes in the encoded proteins, rather it affects most if not all metabolic steps of a spliced RNA including nuclear export[33], degradation[34,35], and translatability[36–39].

Given the importance of RNA regulation in neurodevelopment, one intriguing possibility is that m^6A serves as a dynamic "local code" to regulate local activity-dependent translation[40]. Unlike epigenetic regulation which has a nuclear confinement to histone proteins and DNA, m^6A and other RNA modifications can be carried by RNA molecules and transported into the distal sites of neurons [23,24,41]. In axons, m^6A demethylase FTO is locally translated in response to nerve growth factor, which in turn induces local translation of GAP43 by removing m^6A from GAP43 mRNA and facilitates axonal growth[24]. At synapses, we have previously identified a synaptic m^6A-epitranscriptome

from tripartite synaptosomes in healthy adult mouse forebrains, which consists of nearly 3,000 m^6A-containing transcripts with implications in neurodevelopmental and neuropsychiatric diseases[41]. Among these transcripts, the synaptically hypermethylated transcripts were enriched for synapse functions such as synapse organization and maturation, which is in a sharp contrast to those localized hypomethylated transcripts which are enriched for metabolism (e.g. ribosomal protein subunits, ER, mitochondria). However, no cellular mechanisms responsible for such differential translational regulation, or how this modulatory role is connected to physiology and function of postmitotic neuron development, is known.

The current view holds that the vast majority of m^6A are added to the nascent transcripts in the nucleus. Although the neuronal cytoplasmic readers of m^6A are not completely known today, we have previously shown that three YTH family m^6A readers YTHDF1, YTHDF2, and YTHDF3 are all localized in dendrites, with YTHDF1 having the highest co-localization coefficient with poly(A) RNA. Knocking down YTHDF1 in cultured neurons resulted in immature spines with dampened synaptic transmission and reduced surface expression of AMPA receptors[41]. This *in vitro* result was corroborated by findings in YTHDF1 knockout (KO) mice, which showed dysregulated synaptic transmission and plasticity, and defects in memory consolidation[26]. YTHDF1 has been shown to facilitate translation by recruiting translational initiation factor eIF3, but how this regulation was restricted to a subset of m^6A RNA species is unknown[38]. Recently, the role of m^6A and YTHDF1, YTHDF2, and YTHDF3 proteins in facilitating phase-separation and formation of stress granules has been revealed, indicating another m^6A-mediated mode of translational regulation through self-assemblies of RNA

granules[42]. However, whether this mechanism plays a role in regulating local translation in neurons is currently unknown. Nonetheless, the synaptic transmission and spine morphological deficits in YTHDF1 and YTHDF3 knockdown cells indicated a potential link between the local "m^{6}A decoding" mechanism and synaptopathy observed in neurodevelopmental and neuropsychiatric diseases. What could be the local cellular platforms for m^{6}A regulation in neurons? Can those platforms be targeted by disease-associated genetic variants in humans?

Here we report that cytoplasmic m^{6}A reader YTHDF1 is enriched in neurons and required for axonal, dendritic, and spine development. We show that m^{6}A and YTHDF1 are part of a microtubule plus-end associated RNA granule that contains extensive networks of mRNAs organized by autism risk gene adenomatous polyposis coli (APC). Disrupting m^{6}A signals by knocking down methyltransferase METTL14 or YTHDF1, or overexpressing human autism or schizophrenia-associated missense mutations I311V or S399L in METTL14, reduce expression of APC granules and tubulin, disrupt microtubule assembly and function. These results reveal a novel neuronal subcellular platform where m^{6}A meets with local translation to regulate microtubule dynamics and promote neurodevelopment.

Results

YTHDF1 is a neuronal m^{6}A reader widely expressed in mouse brain

We have previously shown dendritic localization of three cytoplasmic m^{6}A RNA reader proteins YTHDF1, YTHDF2, and YTHDF3[41]. To further identify their cell type-specific expression, we analyzed public sNuc-Seq (single nucleus isolation and RNA

sequencing) dataset from mouse adult hippocampus and found restricted mRNA expression of YTHDF1 (but not YTHDF2 or YTHDF3) to neurons (Fig. 1a, Supplementary Fig. S1a-S1d)[43]. We further confirmed, using double immuno-staining of YTHDF1 and NeuN (pan-neuronal marker) in sagittal mouse brain slices, that YTHDF1 protein is not only widely expressed in the brain but enriched in neurons (NeuN+) (Fig. 1b, Supplementary Fig. S1e). In adult mouse hippocampal CA1, YTHDF1 immuno-staining intensity in pyramidal neurons (NeuN+) was 2-3 times higher than in astrocytes (GFAP+), oligodendrocytes (OLIG2+), or microglia (CX3CR1+) (Fig. 1c-1d). The neuron-enriched expression pattern was retained in dissociated primary hippocampal neuronal cultures, where higher YTHDF1 expression was found in neurons (NeuN+) including excitatory neurons (CaMKII+) and inhibitory neurons (GAD67+), but not in astrocytes (GFAP+), oligodendrocytes (MBP+), or microglia (Iba1+) (Supplementary Fig. S1f-S1g). Thus, cytoplasmic m^6A reader YTHDF1 is enriched in neurons compared to the other major brain cell types.

YTHDF1 is required for post-mitotic development of neurons in culture

To study the role of YTHDF1 in the post-mitotic development of neurons, we first immuno-stained YTHDF1 in GFP-expressing (GFP as a filler) DIV4 mouse hippocampal neurons and observed YTHDF1 in a non-diffused pattern throughout the cytoplasm, including soma, axon, and dendrites (Fig. 1e). We next recapitulated post-mitotic developmental stages with reliable time-windows in primary cultures of hippocampal neurons (e.g. polarization, axonal specification, axon development, dendritic arborization, spine protrusion, and spine maturation), and introduced short-hairpin

knockdown RNAs (shRNA) against YTHDF1 along with EGFP-expression vectors prior to each stage (timepoints shown in Fig. 2a). Significant reduction of YTHDF1 expression (Supplementary Fig. 2a) but unaltered YTHDF2 or YTHDF3, was confirmed. A 19-nt random sequence with no predicted mouse RNA targets was used as negative control (shCtrl).

First, shRNAs were introduced into the dissociated hippocampal neurons using *in vitro* electroporation at DIV0. At DIV4, we fixed the cultures and stained Glu-tubulin (stable microtubule) along with F-actin using Phalloidin-Alexa 568. Compared to shCtrl neurons, significantly less shYTHDF1 neurons had developed dominant axons (a dominant axon is minimally three times longer than others, 63.8% vs. 31.5%) and many neurites lacked a characteristic F-actin “cap” at the axon tip (23.01% in shCtrl vs. 46.4% in sh1 “uncapped”) (Fig. 2b). Thus, reducing YTHDF1 expression at the initial developmental stage compromised neurite specification and outgrowth. Next, we introduced shRNAs along with EGFP at DIV1.5 and fixed the neurons at DIV6. This manipulation did not disrupt the initial neurite development (comparable number of primary neurites including axon in shCtrl and shYTHDF1 at DIV 4, Supplementary Fig. S2b) but severely reduced axonal growth (max length of axonal branch, shCtrl 1498.37 ± 136.41 μm, sh1 591.63 ± 90.65 μm, sh2 1020.39 ± 59.95 μm) and branching (median total axonal branch tip number: 6 in shCtrl, 4 in sh1, and 2 in sh2) were observed at DIV6 (Fig. 2c - 2e) .

To study dendritic development, we delivered shRNAs along with EGFP at DIV3 and fixed cultures at DIV7. shYTHDF1 neurons showed severely underdeveloped dendrites, that were shorter and thinner, showing a “bushy” appearance around frequently deformed soma (Fig. 2f). We performed Sholl analysis to quantify the growth and complexity of dendritic arborization with two parameters: enclosing radius (largest intersecting radius) and sum intersections (total number of points when dendritic branches crossed the concentric circles). YTHDF1-KD neurons showed reduced dendritic lengths (median enclosing radius shCtrl 200.42 ± 11.24 μm, sh1 142.672 ± 10.91 μm, sh2 54.73 ± 4.02 μm) and reduced complexity of dendritic arborization (median sum intersections 1749 ± 134.25 in shCtrl, 662 ± 88.95 in sh1, 292 ± 20.48 in sh2) (Fig. 2g, supplementary Fig. S2c).

Next, we studied the initiation phase of spinogenesis at DIV11-12. YTHDF1 staining puncta were observed throughout dendritic shafts, and inside developing and mature spines at DIV 7, 11, and 18 (Supplementary Fig. S2d). We transfected shRNAs at DIV7 and fixed cultures at DIV12. We omitted sh2 from this experiment because abnormal dendrite arborization was observed (Fig. 2h). Using a classification criterion based on measurements of spine neck and head (see Online Methods), we found that filopodia, the predominant type of spines at this stage, was comparable between shCtrl and shYTHDF1. However, mushroom type of spines shifted to thin spines, another common immature type at this stage (shCtrl 10.82 ± 1.08% mushroom, 29.5 ± 1.33% thin, sh1 4 ± 1.17% mushroom, 35.29 ± 2.35% thin, Fig. 2h-i). A reduction in the spine density was also observed (shCtrl 5.1 ± 0.24 , sh1 3.46 ± 0.24, spines per 10 μm, Fig. 2j).

Finally we delivered shRNAs at DIV14 and fixed cultures at DIV18 to examine spine maturation. No dendritic arborization deficits were detected (Fig. 2k, supplementary fig S2e-g). Compared to DIV12 neurons, mushroom type of spines have become predominant at DIV18 in shCtrl. They are significantly reduced in YTHDF1-KD neurons, concomitantly with an increased proportion of filopodia, indicating that spine maturation requires sufficient YTHDF1 (shCtrl 44.8 ± 1.04% mushroom, 28 ± 1.02% filopodia, shYTHDF1 23.3 ± 1.08% mushroom, 44 ± 1.20% filopodia, Fig.2k-l). Spine density in shYTHDF1 was also reduced (shCtrl 3.6 ± 0.09, shYTHDF1 2.37 ± 0.09, Fig. 2m). The shift from mature to immature types of spines and decreased density in YTHDF1-KD neurons at DIV12 and DIV18 indicates spinogenesis and maturation require YTHDF1 expression.

Knocking down YTHDF1 hampers postnatal development of hippocampal DG neurons *in vivo*

We next sought to investigate *in vivo* cellular phenotypes upon YTHDF1 knockdown using postnatal development of dentate gyrus (DG) granule neurons as a model system. Cre/loxP-mediated inducible shRNA expression vectors targeting YTHDF1 (same target sequences as *in vitro*) were constructed and introduced in combination with vectors expressing either nuclear Cre recombinase (nCre) or tamoxifen-inducible Cre recombinase ($ER^{T2}CreER^{T2}$) into progenitor cells in P0 pups (Fig. 3a-b)[44]. EGFP expression vector was co-introduced for long-term fluorescence labeling. DG neuron development was tested at P7 for differentiation and migration, and at P23 for dendrite and dendritic spine development (Fig. 3b). YTHDF1 reduction was confirmed in vivo

using immunostaining (Supplementary Fig. S3a-b). In shCtrl hippocampus at P7, GFP+ cells were observed in fimbria, dentate notch, CA1-CA3, tertiary dentate matrix (TDM), granule cell layer (GCL) and along the suprafimbrial and subpial migration paths (see annotation in Supplementary Fig. S3c). Strikingly, significantly less shYTHDF1 cells were observed in GCL (shCtrl 7.94 ± 5.79, shYTHDF1 4.98 ± 4.05 cells/slice), and trend of decrease was observed in TDM (shCtrl 6.55 ± 3.83, shYTHDF1 5.09 ± 3.34 cells/slice), indicating deficiency in neurogenesis, migration, and/or survival (Fig. 3c-3d). To investigate dendrite and spine development, we induced Cre activity with three intraperitoneal injections of tamoxifen on days of P17, P18, P19 and sacrificed mice on P23 (Fig 3b). Between shCtrl and shYTHDF1, comparable numbers of DG granules cells had successfully migrated into the two DG blades with no obvious difference in gross dendritic arborization (Supplementary Fig. S4). However, quantification using 3D-Sholl analysis showed significantly reduced complexity upon YTHDF1-KD (Fig. 3f). To further quantify dendrite development, we applied 3D-morphometric analysis using starting point (soma), branching point, and filament tracing to calculate shape, branching patterns, orderliness, and size of dendrites (Fig. 3g). The analysis revealed decreased orderliness (Fig. 3h), reduced straightness (Fig. 3i), less branch depth (Fig. 3j), and larger branching angles (Fig. 3k) in YTHDF1-KD DG neurons, indicating less complex and disordered dendritic arborization. Next, we calculate the physical properties of individual dendrites such as length, diameter, surface area and volume (Fig. 3l). Cumulative distribution curve showed overall thinner and smaller dendrites (Fig. 3m-p). Finally, we applied volumetric analyses to dendritic spines (Fig. 3q) in the outer layer (receiving synaptic input from lateral entorhinal cortex (OL) and middle layer

(receiving synaptic input from medial entorhinal cortex (ML)) and found significantly reduced spine volume (outer layer, shCtrl 0.011 ± 0.01, shYTHDF1 0.009 ± 0.01; middle layer, shCtrl 0.012 ± 0.01, shYTHDF1 0.009± 0.01 μm^3, Fig. 3r-t) and reduced spine density (outer layer, shCtrl 20.1 ± 8.25, shYTHDF1 13.7 ± 3.22 spines/10μm; middle layer, shCtrl 20.5 ± 12.12, shYTHDF1 12.6± 3.70 spines/10 μm, Fig. 3u). Thus *in vivo* results of hippocampal DG neurons consistently showed that YTHDF1 is required for post-mitotic neuron development.

Developmentally regulated APC-RNA granule at the plus-end of the microtubule is enriched with m^6A and associated with YTHDF1

What molecular pathways may be linking dysregulated m^6A function to neurodevelopmental deficits? To identify the potentially involved neuronal RNA granules, we intersected m^6A-mRNA data with PAR-CLIP and HITS-CLIP data for 19 RNA binding proteins (RBPs)[45–48]. Over-representation of m^6A-mRNA was found in three RBP granules compared to others: fragile X mental retardation protein (FMRP, a potential m^6A reader protein), adenomatous polyposis coli (APC), and neuro-oncological ventral antigen (NOVA) (Fig. 4a). Given that APC is known as a microtubule plus-end tracker and involved in local translation of many cytoskeletal components and regulators, we reasoned that its dysfunction can be a strong candidate for explaining the developmental deficits in YTHDF1-KD neurons[45,49]. Not only all developmental stages of neurons require functional microtubules, the spine deficits we observed were reminiscent to those under low-dose nocodazole treatment[50]. Hypergeometric gene enrichment analysis confirmed that m^6A-modified mRNA was significantly enriched in

APC-bound mRNAs (representation factor 1.4; p =2.592e-10, Fig. 4b) and topological distribution of m^6A sites in the APC-bound m^6A-mRNAs showed 50% sites in CDS and 39% sites in 3'UTR (Fig. 4c). m^6A RNA dot-blot following APC immunoprecipitation confirmed enriched m^6A (three times enrichment over input RNA) but not poly(A) (Fig. 4d; Supplementary Fig. S5). Many m^6A-mRNAs in APC granules, including Tubb2b, Ctnnb1, Cdc42 and more, are known to be developmentally regulated[49]. To understand whether m^6A status in APC granule is dynamic, we performed gene expression and differential methylation (DM) analyses on APC and APC-targeted mRNAs at embryo day 13 (E13), postnatal day 14 (P14), and adult mice cortex using published MeRIP-seq databases[31,51]. Normalized expression z scores of APC mRNA and 274 APC-bound mRNAs showed that the majority of these mRNAs were downregulated in adulthood (Fig. 4e, Supplementary Table S1). Next, we used the methylation analysis package RADAR to call DMs on APC mRNA and APC bound mRNAs[52]. 1,921 DM loci in 188 mRNAs (FDR < 0.05 & |log2FC| >= 0.5) were detected (note 8 DM loci were mapped to protocadherin (Pcdh) gene clusters with annotation ambiguity. We have listed all 30 Pcdh annotation candidate genes in Supplementary table S2). Of 1,921 loci, 284 (in 97 mRNAs) were detected at P14 versus E13 (181 down, 103 up). 1,709 DM loci (in 188 mRNAs) were detected at adult versus E13 (1,309 down, 400 up) (Fig. 4f, Supplementary table S2). We next used DESeq2 (FDR<0.05 AND |log2FC| >= 1) to call differential expression (DE) status of the 188 mRNA with DMs. In Fig 4f, The left two columns depict the log2FC of methylation scores of DMs and the right two columns depict log2FC of corresponding mRNA expression in respective developmental timepoints. The log2FC values are sorted in ascending order from right to left ("NA":

non-differential). The sorted alignment showed that methylation dynamics is not in parallel relation to the gene expression level of these mRNAs (Fig. 4f). Three examples of regulated DM loci in Tbr1, Ctnnb1, and Tubb2b mRNAs were depicted for their methylation and transcripts dynamics (Fig. 4g). Thus, mRNAs in APC-RNA granules are developmentally regulated, at both mRNA level and methylation level.

What m^6A regulators may also reside in APC granules? APC immunoprecipitation followed by immuno-blotting showed no evidence of m^6A methyltransferases (METTL3 and METTL14) or demethylases (FTO and ALKBH5) in the complex. Out of three cytoplasmic m^6A readers (YTHDF1, YTHDF2, and YTHDF3), YTHDF1 was co-immunoprecipitated with APC (Fig. 4h). To understand the nature of this interaction, we pre-treated cell lysate with RNase A before APC immunoprecipitation, which resulted in a significant reduction in co-immunoprecipitated YTHDF1, eukaryotic translation initiation factors eIF3A and eIF3B, and small ribosomal subunit RPS19, suggesting that their interactions with APC were RNA-mediated (Fig. 4i). To confirm the interaction in situ, we co-stained APC and YTHDF1 in cultured neurons. Since APC is a large, unstructured protein extending over 600 nm per APC molecule, we rendered APC-RNA granules as 600 nm spheres, and asked whether YTHDF1 was in their peripheral. We observed that 81.36 ± 3.63% and 89.14 ± 1.69% spheres were in contact with YTHDF1 signal in axons and dendrites respectively (Fig. 4j). Thus, YTHDF1 is associated with APC granules and may play a role in “interpreting” m^6A signals on the APC-bound mRNAs.

Knocking down m^{6}A writer METTL14 or APC caseud neuronal phenotypes resembling YTHDF1-KD

Next, we tested whether there is functional overlap between m^{6}A modification and its decoding by YTHDF1 and APC during neurodevelopment. Thus we repeated our knock-down experiments in cultured hippocampal neurons using shRNAs against methyltransferase METTL14 (see Fig. S6a for KD efficiency), YTHDF1, and APC (see Fig. S6b for KD efficiency,). In parallel experiments, we overexpressed FTO, an m^{6}A demethylase to reduce m^{6}A level (Fig. 5a). Similarly to YTHDF1, knocking down METTL14 or APC resulted in drastically reduced axonal length as well as branching (Fig. 5b, Supplementary table S3). Overexpressing FTO however promoted axonal growth as indicated by both max length and number of branching tips (Fig. 5b-d, Supplementary table S3). The result of FTO in axon development is consistent with its previously reported role in promoting axon elongation through local translation of GAP-43, an m^{6}A modified mRNA not in APC-RNA granule[24]. For dendritic development, Sholl analysis revealed severely disrupted dendritic growth upon knocking down METTL14, or YTHDF1, or APC (Fig. 5e-g, Fig. S6c-k, Supplementary table S3). However, overexpression of FTO exerted no effect to dendrite development (Fig. 5e-g, Supplementary table S3). Thus in both developing axons and dendrites, knocking down m^{6}A writer METTL14 or reader YTHDF1 shows consistent phenotypes with APC-KD in hampering neurodevelopment.

METTL14 and YTHDF1 are required for APC-RNA granule expression and microtubule function

Is the resemblance in neurodevelopmental phenotypes between YTHDF1-KD, METTL14-KD, and APC-KD a coincidence? Alternatively, are m^6A and YTHDF1 involved in regulating APC granules? Previously, we detected reduction of APC immunoreactivity in YTHDF1-KD neurons[41]. Now, using two more shRNAs against YTHDF1, as well as shRNAs against METTL14, we observed reduced expression of APC-RNA granules not only in YTHDF1-KD neurons, but also in METTL14-KD neurons (YTHDF1-KD: shCtrl 48.58± 3.57, sh1 34.51 ± 2.14, sh2 28.99 ± 1.65; METTL14-KD: sh1 39.269 ± 1.56 sh2 34.042 ± 1.37 A.U.), indicating m^6A signal is required for APC granule expression in developing neurons (Fig. 6a-b). Since APC is known responsible for local synthesis of microtubule subunit β2B-tubulin (Tubb2b)[45], we asked whether expressions of Tubb2b and other microtubule protein components are altered. Immunostaining against Tubb2b, Tyrosine-tubulin (Tyr-tub, dynamic tubulin), and neuron-specific microtubule-associated protein 2 (MAP2) showed significant reduction in YTHDF1-KD or METTL14-KD neurons, both in soma and in dendrites, indicating an essential role of m^6A signal in synthesizing microtubule components and composition (Fig. 6c-d). Not only the composition of microtubule, but the structure of microtubule, was disrupted, as exemplified in the “microtubule debundling” phenomenon adjacent to soma (Fig. 6e). Finally, a characteristic morphological phenotype for loss of function of APC, “collapsed” growth cones, caused by losing the dynamic peripheral domain of growth cones (in contrast to the “intact” fan-shaped growth cones), was observed in YTHDF1-KD, METTL14-KD and APC-KD neurons. Neurons with any one of these three proteins being knocked down had larger populations of “collapsed” type of growth cones in contrast to the “intact” fan-shaped growth cones (intact/collapsed ratio 1.36 in shCtrl,

0.07 in YTHDF1-sh1, 0.17 in YTHDF1-sh2, 0.24 in METTL14-sh1, 0.26 in METTL14-sh2, 0.12 in APC-sh2, 0.10 in APC-sh3, Fig. 6f-g) as well as reduced growth cones area (Median: shCtrl 9.76 ± 0.81 μm^2, METTL14-sh1 5.89 ± 0.98 μm^2, METTL14-sh2 4.58 ± 0.44 μm^2, YTHDF1-sh1 3.87 ± 0.35 μm^2, YTHDF1-sh2 4.82 ± 0.53 μm^2, APC-sh2 4.22 ± 1.25 μm^2, APC-sh3 4.76 ± 0.83 μm^2, Fig. 6h). Thus, dendritic APC granule expression, which is important for synthesizing and regulating dynamic microtubules, requires both m^6A expression and its reader protein YTHDF1.

Overexpressing m^6A demethylase FTO, which did not inhibit neurodevelopment, did not affect APC immunoreactivity (Supplementary Fig. S7a-c). Furthermore, none of the 56 hypermethylated RNAs in FTO cKO mice was identified as APC target mRNAs[29] (Supplementary Fig. S7d). This result is consistent with lack of FTO detection in APC immunoprecipitates and suggests that demethylation activity by FTO is not required for regulating APC granule expression or function.

Autism and Schizophrenia-associated mutations in METTL14 impact APC expression and neuron development

Human genetic variations affecting microtubule dynamic and neuron development have been associated with neurodevelopmental and neuropsychiatric diseases, including APC as autism and schizophrenia risk gene[53–55]. Identifying APC granules at the dynamic end of microtubule as a highly m^6A-modified ribonucleoprotein complex which are associated with m^6A and YTHDF1 suggests that genetic or environmental stimuli that disrupt m^6A function may have pathological consequences. In The Human Gene

Mutation Database (HGMD), we found two METTL14 missense mutations (NM_020961.3: 931A>G; NP_066012.1: I311V, phenotype="Autism" & NM_020961.3: 1196C>T; NP_066012.1: S399L, phenotype= “Schizophrenia”)[56], whose cellular functions are unknown. First we mapped the two affected amino acids to the protein structure of human METTL3/METTL14 methyltransferase core complex. Both I311 and S399 were mapped to the interface between METTL3 and METTL14 (Fig. 7a). D312, next to I311, has been shown as a key residue for methylation activity and substrate selectivity[57,58]. Simulated molecular interaction after replacing isoleucine with valine, the mutant form associated with autism, suggested that the number of residues in METTL3 with hydrophobic interaction with V311 would reduce (Fig. 7b). S399 is shown in the protein structure as a phosphorylated amino acid that forms salt bridge with R471 in METTL3. Leucine (L399), the schizophrenia-associated mutant form, would disrupt this interaction through loss of the complementary negative charge. Since m^6A methylation activity requires both catalytic activity by METTL3 and allosteric support by METTL14, these mutations in METTL14 can be predicted to comprise methylation performance. We reasoned that if the mutations cause non-functional METTL14 (e.g. unstable and/or unable to interact with METTL3), overexpression of these mutants in neurons will cause no harm. However, if the mutations cause gain of adverse function, phenotypic consequences may be observed. Toward this end, we first identified the equivalent amino acid replacement in the mouse ortholog of METTL14 (99% identical to human at amino acid level), and performed mutagenesis in full-length mouse cDNA to introduce I311V and S399L. Then we overexpressed the mutants in cultured rodent primary hippocampal neurons and measured their impact on m^6A expression and

neurodevelopment. We stained APC in these neurons simultaneously to investigate whether the phenotypic changes can be associated with APC granule expression (Fig. 7c). As shown in Fig. 7d, Sholl analysis showed that overexpression of mutated but not wild-type METTL14 resulted overall shorter dendrites with less complexity (median enclosing radius: Empty 152.59 ± 8.29 μm, WT 144.95 ± 9.93 μm, I311V 105.50 ± 6.90 μm, S399L; 116.51 ± 4.83 μm; interpolated median sum intersections: Empty 2156 ± 177.23, WT 2338 ± 135.14, I311V 1561 ± 109.85, S399L 1763 ± 89.95), demonstrating that the disease-associated mutations, not the excessive amount of METTL14, causes dendritic developmental deficits. Furthermore, we found reduced immunoreactivity of APC protein in soma (Fig. 7e) and reduced APC puncta intensity in dendrite (Fig. 7c, f), indicating APC granule expression is inhibited by these mutations. Consistent with the molecular deficits, overexpression of I311V and S399L resulted in “collapsed” dendritic growth cones (area: Empty 11.78 ± 1.03 μm^2, WT 11.75 ± 1.91 μm^2, I311V 5.73 ± 0.51 μm^2, S399L 6.48 ± 0.52 μm, Fig. 7g-7h). Furthermore, immunostaining showed reduced dynamic microtubule Tyr-tubulin (staining intensity A.U.: Empty 62.58 ± 2.97, WT 68.19 ± 1.74, I311V 53.38 ± 2.83, S399L 54.84 ± 2.67), but unaltered MAP2 immunoreactivity (Fig. 7i-k). These results suggest mutations I311V and S399L in METTL14 gain potentially pathogenic functions and impact APC granules and neuronal microtubules.

Finally, we tested whether the methyltransferase with I311V or S399L mutant METTL14 subunits is functional for supporting neurodevelopment. We overexpressed wild-type or mutant METTL14 in METTL14-KD neurons and measured the impact on dendrite development. The shRNA-resistant wild-type METTL14 successfully rescued both

METTL14 expression and dendrite development; mutant METTL14 partially rescued dendrite development as measured by Sholl analysis, to a lesser level compared to wild-type METTL14 (Fig. 7l-7m). The recovery of dendrite development was ranked 'WT > I311V > S399L > No rescue', indicating that the mutant METTL14 proteins are partially functional; however, intact function is required for neurodevelopment. Importantly, reduced APC expression was also partially rescued by overexpressing I311V or S399L METTL14 mutants (Fig. 7n).

Discussion

A critical goal of this study is to identify the role of m^6A in post-mitotic neurodevelopment through temporal and spatial RNA regulation pathways. Previously, m^6A has been shown to be involved in cortical neurogenesis through conferring rapid turnover of m^6A tagged transcripts to control transcriptome composition[21,22]. Local function of m^6A has been shown in axon growth and guidance involving regulated local translation, a core mechanism for neurodevelopment and a convergent target in neurodevelopmental, neuropsychiatric, and neurodegenerative diseases[16,20,23,24].

Thousands of m^6A modified mRNAs have been identified in the neuronal processes[41], posing the complexity and challenge of identifying function-specific regulation. Associating select sets of m^6A RNAs to specific neuronal RNA granules offers one approach to achieve further spatiotemporal resolution and specific functional relevance. In this study, not only we identify the role of m^6A and its reader protein YTHDF1 in regulating post-mitotic neurodevelopment, we show they are associated with APC granule, a self-organized local translatome at the plus-end of microtubules, as a

potential mechanism to direct m^6A-mediated protein synthesis to specific subcellular locations.

An outstanding question is how m^6A and its reader YTHDF1 engage APC granules to target protein synthesis to the plus-end of microtubule. Previously, we showed APC mRNA in neuronal dendrites, whose stability and dendritic localization were not, but translation was dependent on YTHDF1 (Merkurjev et al., 2018). Current data consistently show decreased APC immunoreactivities in soma and dendrites after knocking down YTHDF1, or METTL14, or overexpressing disease-associated METTL14 mutants (I311V and S399L), suggesting APC protein expression is highly dependent on intact m^6A activity. APC has been shown to play a pivotal role in brain development such as cortical layer formation and axonal tract development, consistent with the phenotypes we have observed in YTHDF1-KD neurons. Single nucleotide polymorphism in the 3' UTR of transcribed RNA, heritable germline mutations, and aberrant chromosomal localization of APC gene are associated with pervasive neuro-cognitive dysfunction in human, including autism and schizophrenia[53–55]; thus dysregulated expression of APC at transcription or post-transcriptional level can both lead to pathogenic brain structures and cognitive function. As APC is the "hub" protein in the APC granules, its dysregulated expression automatically leads to the mal function of the granule, thus it is difficult to disentangle the role of m^6A and YTHDF1 on APC expression from its role on APC granule function. Previous studies demonstrated the function of APC granules in promoting Tubb2b expression, by using specific morpholino oligonucleotides to disrupt association of Tubb2b mRNA to APC. This experiment resulted in deficits in Tubb2b expression, microtubule and growth cone function[45]. We

suspect that m^6A and its reader YTHDF1 are not only required for APC expression, but also for expression of APC-bound mRNAs, locally. The high enrichment of m^6A in APC-bound mRNAs and local presence of YTHDF1 in close proximity of APC-granules in both developing axons, dendrites, and growth cones support this view. Furthermore, APC cKO mice showed increased axonal branching and spine density, increased frequency of miniature excitatory synaptic currents, and long-term potentiation[59,60] , thus missing APC function alone and possible consequences on the APC granules do not fully account for the YTHDF1-KD phenotypes.

However, to understand the role of m^6A and YTHDF1 in APC granules, and furthermore how this local epitranscriptomic regulation is linked to physiology and function of neurons, experiments to disrupt specific m^6A sites and association of YTHDF1 to APC-bound mRNAs have to be done. As the binding sites in APC-bound mRNAs are predominantly in 3'UTR with motifs distinct from m^6A canonical motif, it is unlikely APC uses m^6A marks to recruit mRNAs into the granules[45]. m^6A signal is transcript-, position- and context-dependent, thus multiple individual mRNAs have to be studied to reveal the nature of this regulation mechanism. We showed several genes such as Tbr1, Ctnnb1, and Tubb2b, whose mRNAs are developmentally regulated, both at transcript level, and at methylation level. These mRNAs can make an initial investigation list once their m^6A sites are specified. Until then, the full responsibility of epitranscriptomic regulation on APC granule remains elusive; nonetheless, the neurodevelopmental deficits associated with YTHDF1 knockdown is consistent with the role of APC in microtubule assembly, growth cone function, polarity establishment, neuron migration, and synapse formation[45].

Another intriguing mechanism involves the role of m^6A and m^6A reader proteins in promoting phase-separation and protein-RNA assembly. Such a process has been recently suggested in neuronal transport granule formation and translational activation[42]. Thus the deficits we have observed could have potentially originated from a failure of APC-RNA granule assembly, or a failure of translation, or both, with the two processes possibly mutually dependent. Another alternative explanation for the phenotype is transportation deficits associated with microtubule malassembly[61], suggested by the debundling in primary dendrites and reduced MAP2 staining. Neuronal microtubules not only provide structural and mechanical support, serve as transportation tracks, but also organize local signaling events such as translation itself. Not only components of translational machinery are associated with cytoskeleton in a wide range of cells and organisms, pharmacological treatments have shown that bulk protein synthesis is dependent on cytoskeletal integrity. With all of these mechanisms potentially involved in the reduction of APC granules upon dysregulation of m^6A, a full understanding of the role of m^6A in APC granules remains a future challenge, including identifying new components in the granule responsible for activity-dependent responses.

Remarkably, the YTHDF1-KD phenotype in neurodevelopment we have observed are consistent with but more severe than those in YTHDF1 germline knockout mice[26] and striatum-specific METTL14 knockout mice[62]. This phenotype diversity could be associated with the modulatory role of m^6A that can be compensated with transcriptional and post-transcriptional plasticity, or protein feedback loops as recently reported[63]. Moreover, the context where loss of function of YTHDF1 or METTL14 has occurred can also be important for the functional outcome. Molecular manipulations with high spatial

and temporal resolution and high specificity will be essential for delineating the function of m^6A and its readers..

Other local RNA granules involved in neurodevelopment and synaptic plasticity may also require m^6A-mediated translational regulation. Fragile X mental retardation protein (FMRP), a local translation repressor of many synaptic proteins was identified in an unbiased candidate search as a m^6A reader protein[64], raising the possibility that m^6A-RNA accumulates in FMRP granules and they are translationally repressed during the transport and activated upon group I mGluR activation. A recent report showed that FMRP facilitates m^6A-dependent mRNA nuclear export and modulates neural differentiation[22], however the local translational regulation in the context of synaptic plasticity of FMRP-m^6A RNPs has not been demonstrated. Other types of granules that m^6A has been associated with are stress granules and P-bodies[42], however the transcript selectivity in these RNPs and their relation to neurodevelopment are unclear. APC granules that we have established to be associated with m^6A and its reader protein YTHDF1, are associated with developing neurons as we show many of its bound mRNAs of functional cohort are downregulated in adult brains.

Finally, how does human disease-associated METTL14 mutations cause the functional deficits of APC-RNA granules and neurodevelopment? m^6A methyltransferases consists of a heterodimer of METTL3 and METTL14 together with other factors to confer site-specific methylation activity. Although METTL3 is the catalytic subunit, METTL14 plays a critical role in substrate recognition as well as provides allosteric support required by METTL3 for its catalytic activity. D312A mutation in METTL14 has previously been reported as to partially disrupt the interaction between METTL3 and

METTL14, but drastically reduce methylation activity[58]. R298P in METTL14 not only reduces methylation activity but also abolishes substrate selectivity[58]. The Autism and Schizophrenia mutations we investigated in this study, I311V and S399L, are located close to these reported mutation sites, suggesting that they may also affect interaction between METTL3 and METTL14, thus impair catalytic function of METTL3. The similarity to METTL14-knockdown phenotypes (e.g. reduced APC expression, disrupted microtubule assembly, and hampered dendritic development), suggest a functional downregulation. One possibility is that mutant METTL14 can not form stable heterodimer with METTL3, but retains recognition capability of RNA substrates, thus "binds away" RNA substrates from METTL3 catalytic activity. Another possibility is that mutant METTL14 can still bind to RNA and METTL3, but can not provide the required allosteric support thus impairs methylation activity. The primary pathogenic causes however are yet unclear and warrant future investigation in neurons and other brain cell types. Given that both autism and schizophrenia are etiologically complex diseases and polygenic, future studies using iPS-derived cell models for neuropsychiatric diseases may become highly relevant.

Many more questions can be raised from the links between APC granule and m^6A epitranscriptomic regulation, and neurodevelopmental diseases, such as how APC-m^6A granules produce activity-dependent translational responses and microtubule remodeling accordingly. m^6A-mediated translation regulation has been shown to be stimulus-induced such as depolarization in neurons[26]. This finding is consistent with dynamic m^6A regulation in a wide context such as learning and memory[26,27], stress[31], axon growth[23], and spinal injury[32], with their underlying cellular pathways yet to be

discovered. Although APC-m^{6}A RNA granules are promising candidates for epitranscriptomic regulation in neurons, we suspect more RNA granules to be discovered in neurons and other cell-types. It will also be interesting to understand how these pathways help build individual brains of different levels of cognitive capability and resilience to environmental challenges, such as stress.

METHODS

Methods, including statements of data availability and any associated references, are available at https://doi.org/XXXXX.

Acknowledgments.

We thank Wayne Sossin for the critical reading of this manuscript. We thank Dr. Masayuki Taniguchi and Dr. Tomoyuki Furuyashiki (Kobe University) for the frozen brain tissue of CX3CR1-GFP mice. We thank Dr. Fumiyoshi Ishidate at the CeMI imaging center at iCeMS and Hiroki Umeshima at Tokushima university for technical support. We thank Dr. Soundhar Ramaswamy for scRNA-seq meta-analysis. This work was supported by KAKENHI 17H03546, 19H04907, 19H05212, AMED 18dm0307023h 0001, NSFC 31971335, Xingliao Talents Program, XLYC1802007, Department of Education of Liaoning Province1911520092, Hirose research grant, Takeda research grant to DOW. Sasakawa research grant to R.R. and M.S.. R.R is supported by the Mitsubishi scholarship and JASSO Honor Fellowship. KOL is supported in part by the Research Grant Council of Hong Kong [General Research Fund (GRF) 17135816]

Author Contributions

D.O.W, X.L, and R.R conceived and designed the project. R.R, I.O. and R.F performed knock-down experiments in vitro. X.L, S.H and R.R performed overexpression, rescue experiments, and data analyses. I.O performed co-localization imaging. W.T.H performed Western blotting, immunoprecipitation, RNA extractions and m^6A dot-blot. S.H, R.R. performed immunostaining and spine analysis. Y.F. subcloned cDNA and constructed expression plasmids, shRNA plasmids, performed Western blotting, mutation mappings and molecular simulation, M.S, H.I, and S.H performed *in vivo* electroporation and analyzed data. K.J. Performed computational analysis of m^6a-seq datasets. D.O.W. and R.R. wrote the manuscript. K. N and K.O.L supervised parts of the project. All authors made indispensable contributions.

Conflict of interests

The authors claim no conflict of interests.

References:

1. Terenzio, M., Schiavo, G. & Fainzilber, M. Compartmentalized Signaling in Neurons: From Cell Biology to Neuroscience. *Neuron* **96**, 667–679 (2017).
2. Lennox, A. L., Mao, H. & Silver, D. L. RNA on the brain: emerging layers of post-transcriptional regulation in cerebral cortex development. *Wiley Interdiscip Rev Dev Biol* **7**, (2018).
3. Roy, R., Shiina, N. & Wang, D. O. More dynamic, more quantitative, unexpectedly intricate: Advanced understanding on synaptic RNA localization in learning and memory. *Neurobiology of Learning and Memory* **168**, 107149 (2020).

4. Holt, C. E., Martin, K. C. & Schuman, E. M. Local translation in neurons: visualization and function. *Nat Struct Mol Biol* **26**, 557–566 (2019).
5. Shigeoka, T. *et al.* Dynamic Axonal Translation in Developing and Mature Visual Circuits. *Cell* **166**, 181–192 (2016).
6. Hengst, U., Deglincerti, A., Kim, H. J., Jeon, N. L. & Jaffrey, S. R. Axonal elongation triggered by stimulus-induced local translation of a polarity complex protein. *Nat Cell Biol* **11**, 1024–1030 (2009).
7. Bestman, J. E. & Cline, H. T. The RNA binding protein CPEB regulates dendrite morphogenesis and neuronal circuit assembly in vivo. *Proc Natl Acad Sci U S A* **105**, 20494–20499 (2008).
8. Bramham, C. R. & Wells, D. G. Dendritic mRNA: transport, translation and function. *Nat Rev Neurosci* **8**, 776–789 (2007).
9. Antar, L. N., Li, C., Zhang, H., Carroll, R. C. & Bassell, G. J. Local functions for FMRP in axon growth cone motility and activity-dependent regulation of filopodia and spine synapses. *Mol Cell Neurosci* **32**, 37–48 (2006).
10. Kiebler, M. A. & Bassell, G. J. Neuronal RNA granules: movers and makers. *Neuron* **51**, 685–690 (2006).
11. Richter, J. D. & Klann, E. Making synaptic plasticity and memory last: mechanisms of translational regulation. *Genes Dev.* **23**, 1–11 (2009).
12. Wang, E. T. *et al.* Dysregulation of mRNA Localization and Translation in Genetic Disease. *J. Neurosci.* **36**, 11418–11426 (2016).
13. Huber, K. M., Klann, E., Costa-Mattioli, M. & Zukin, R. S. Dysregulation of Mammalian Target of Rapamycin Signaling in Mouse Models of Autism. *J Neurosci* **35**, 13836–13842 (2015).
14. Rosina, E. *et al.* Disruption of mTOR and MAPK pathways correlates with severity in idiopathic autism. *Transl Psychiatry* **9**, 50 (2019).

15. Szaro, B. G. & Strong, M. J. Post-transcriptional control of neurofilaments: New roles in development, regeneration and neurodegenerative disease. *Trends in Neurosciences* **33**, 27–37 (2010).

16. Wang, D. O. RNA Modifications in the Central Nervous System. in *The Oxford Handbook of Neuronal Protein Synthesis* (ed. Sossin, W. S.) (Oxford University Press, 2020). doi:10.1093/oxfordhb/9780190686307.013.23.

17. Dunin-Horkawicz, S. *et al.* MODOMICS: a database of RNA modification pathways. *Nucleic Acids Res* **34**, D145–D149 (2006).

18. Shi, H., Wei, J. & He, C. Where, when and how: context-dependent functions of RNA methylation writers, readers, and erasers. *Mol Cell* **74**, 640–650 (2019).

19. Satterlee, J. S. *et al.* Novel RNA modifications in the nervous system: form and function. *J Neurosci* **34**, 15170–15177 (2014).

20. Livneh, I., Moshitch-Moshkovitz, S., Amariglio, N., Rechavi, G. & Dominissini, D. The m 6 A epitranscriptome: transcriptome plasticity in brain development and function. *Nature Reviews Neuroscience* **21**, 36–51 (2020).

21. Yoon, K.-J. *et al.* Temporal Control of Mammalian Cortical Neurogenesis by m6A Methylation. *Cell* **171**, 877-889.e17 (2017).

22. Edens, B. M. *et al.* FMRP Modulates Neural Differentiation through m6A-Dependent mRNA Nuclear Export. *Cell Reports* **28**, 845-854.e5 (2019).

23. Zhuang, M. *et al.* The m6A reader YTHDF1 regulates axon guidance through translational control of Robo3.1 expression. *Nucleic Acids Res* **47**, 4765–4777 (2019).

24. Yu, J. *et al.* Dynamic m6A modification regulates local translation of mRNA in axons. *Nucleic Acids Research* **46**, 1412–1423 (2018).

25. Fustin, J.-M. *et al.* RNA-Methylation-Dependent RNA Processing Controls the Speed of the Circadian Clock. *Cell* **155**, 793–806 (2013).

26. Shi, H. *et al.* m6A facilitates hippocampus-dependent learning and memory through

YTHDF1. *Nature* **563**, 249–253 (2018).

27. Widagdo, J. *et al.* Experience-Dependent Accumulation of N^6-Methyladenosine in the Prefrontal Cortex Is Associated with Memory Processes in Mice. *J. Neurosci.* **36**, 6771–6777 (2016).

28. Walters, B. J. *et al.* The Role of The RNA Demethylase FTO (Fat Mass and Obesity-Associated) and mRNA Methylation in Hippocampal Memory Formation. *Neuropsychopharmacol* **42**, 1502–1510 (2017).

29. Hess, M. E. *et al.* The fat mass and obesity associated gene (Fto) regulates activity of the dopaminergic midbrain circuitry. *Nat Neurosci* **16**, 1042–1048 (2013).

30. Wang, L. *et al.* Genetic Variants in the Fat Mass- and Obesity-Associated (FTO) Gene are Associated with Alcohol Dependence. *J Mol Neurosci* **51**, 416–424 (2013).

31. Engel, M. *et al.* The Role of m6A/m-RNA Methylation in Stress Response Regulation. *Neuron* **99**, 389-403.e9 (2018).

32. Weng, Y.-L. *et al.* Epitranscriptomic m6A Regulation of Axon Regeneration in the Adult Mammalian Nervous System. *Neuron* **97**, 313-325.e6 (2018).

33. Roundtree, I. A. *et al.* YTHDC1 mediates nuclear export of N6-methyladenosine methylated mRNAs. *eLife* **6**,.

34. Wang, X. *et al.* N6-methyladenosine-dependent regulation of messenger RNA stability. *Nature* **505**, 117–120 (2014).

35. Zaccara, S. & Jaffrey, S. R. A Unified Model for the Function of YTHDF Proteins in Regulating m6A-Modified mRNA. *Cell* **181**, 1582-1595.e18 (2020).

36. Meyer, K. D. *et al.* 5′ UTR m6A Promotes Cap-Independent Translation. *Cell* **163**, 999–1010 (2015).

37. Coots, R. A. *et al.* m6A Facilitates eIF4F-Independent mRNA Translation. *Mol Cell* **68**, 504-514.e7 (2017).

38. Wang, X. *et al.* N6-methyladenosine Modulates Messenger RNA Translation Efficiency.

Cell **161**, 1388–1399 (2015).

39. Zhou, J. *et al.* Dynamic m6A mRNA methylation directs translational control of heat shock response. *Nature* **526**, 591–594 (2015).

40. Madugalle, S. U., Meyer, K., Wang, D. O. & Bredy, T. W. RNA N6-Methyladenosine and the Regulation of RNA Localization and Function in the Brain. *Trends Neurosci* (2020) doi:10.1016/j.tins.2020.09.005.

41. Merkurjev, D. *et al.* Synaptic N6-methyladenosine (m6A) epitranscriptome reveals functional partitioning of localized transcripts. *Nat. Neurosci.* **21**, 1004–1014 (2018).

42. Ries, R. J. *et al.* m 6 A enhances the phase separation potential of mRNA. *Nature* **571**, 424 (2019).

43. Habib, N. *et al.* Div-Seq: Single-nucleus RNA-Seq reveals dynamics of rare adult newborn neurons. *Science* **353**, 925–928 (2016).

44. Ito, H., Morishita, R., Iwamoto, I. & Nagata, K. Establishment of an in vivo electroporation method into postnatal newborn neurons in the dentate gyrus. *Hippocampus* **24**, 1449–1457 (2014).

45. Preitner, N. *et al.* APC is an RNA-Binding Protein and its Interactome Provides a Link to Neural Development and Microtubule Assembly. *Cell* **158**, 368 (2014).

46. Hafner, M. *et al.* Transcriptome-wide identification of RNA-binding protein and microRNA target sites by PAR-CLIP. *Cell* **141**, 129–141 (2010).

47. Ascano, M., Jr *et al.* FMRP targets distinct mRNA sequence elements to regulate protein expression. *Nature* **492**, 382–386 (2012).

48. Schwartz, S. *et al.* Perturbation of m6A writers reveals two distinct classes of mRNA methylation at internal and 5' sites. *Cell Rep* **8**, 284–296 (2014).

49. Shigeoka, T. *et al.* Dynamic Axonal Translation in Developing and Mature Visual Circuits. *Cell* **166**, 181–192 (2016).

50. Jaworski, J. *et al.* Dynamic Microtubules Regulate Dendritic Spine Morphology and

Synaptic Plasticity. *Neuron* **61**, 85–100 (2009).

51. EMBL-EBI. ENA Browser. https://www.ebi.ac.uk/ena/browser/view/PRJNA595356.

52. Zhang, Z. *et al.* RADAR: differential analysis of MeRIP-seq data with a random effect model. *Genome Biology* **20**, 294 (2019).

53. Zhou, X.-L. *et al.* Association of adenomatous polyposis coli (APC) gene polymorphisms with autism spectrum disorder (ASD). *American Journal of Medical Genetics Part B: Neuropsychiatric Genetics* **144B**, 351–354 (2007).

54. Cruz-Correa, M. R. *et al.* Ubiquitous neurocognitive dysfunction in familial adenomatous polyposis: proof-of-concept of the role of APC protein in neurocognitive function. *Hered Cancer Clin Pract* **18**, 4 (2020).

55. Cui, D. H., Jiang, K. D., Jiang, S. D., Xu, Y. F. & Yao, H. The tumor suppressor adenomatous polyposis coli gene is associated with susceptibility to schizophrenia. *Molecular Psychiatry* **10**, 669–677 (2005).

56. Human Gene Mutation Database. in *Encyclopedia of Genetics, Genomics, Proteomics and Informatics* (ed. Rédei, G. P.) 921–921 (Springer Netherlands, 2008). doi:10.1007/978-1-4020-6754-9_7919.

57. Wang, X. *et al.* Structural basis of N6-adenosine methylation by the METTL3–METTL14 complex. *Nature* **534**, 575–578 (2016).

58. Wang, P., Doxtader, K. A. & Nam, Y. Structural Basis for Cooperative Function of Mettl3 and Mettl14 Methyltransferases. *Molecular Cell* **63**, 306–317 (2016).

59. Chen, Y., Tian, X., Kim, W.-Y. & Snider, W. D. Adenomatous Polyposis Coli Regulates Axon Arborization and Cytoskeleton Organization via Its N-Terminus. *PLoS One* **6**, (2011).

60. Mohn, J. *et al.* Adenomatous polyposis coli protein deletion leads to cognitive and autism-like disabilities. *Mol Psychiatry* **19**, 1133–1142 (2014).

61. Baumann, S. *et al.* A reconstituted mammalian APC-kinesin complex selectively transports defined packages of axonal mRNAs. *Sci Adv* **6**, (2020).

62. Koranda, J. L. *et al.* Mettl14 Is Essential for Epitranscriptomic Regulation of Striatal Function and Learning. *Neuron* **99**, 283-292.e5 (2018).

63. El-Brolosy, M. A. *et al.* Genetic compensation triggered by mutant mRNA degradation. *Nature* **568**, 193–197 (2019).

64. Zhang, F. *et al.* Fragile X mental retardation protein modulates the stability of its m6A-marked messenger RNA targets. *Human Molecular Genetics* (2018) doi:10.1093/hmg/ddy292.

Figure and table legends:

Figure 1. YTHDF1 is a neuronal m^{6}A reader widely expressed in mouse brain

a. Single-cell mRNA expression of m^{6}A readers *Ythdf1*, *Ythdf2*, and *Ythdf3* in adult mouse hippocampus. **b.** Immunofluorescence images of mouse whole brain slice (postnatal 20 weeks) merging YTHDF1 (green) and NeuN (red). Scale bar 500 μm. **c.** Confocal images of hippocampal CA1 (postnatal 15 weeks) of wild type or CX3CR1-GFP mouse stained with YTHDF1 (red) with pan-neuronal marker NeuN or astrocyte marker GFAP or oligodendrocyte marker Olig2 (green), and nuclear marker DAPI (blue). Arrows pointing at representative cells in YTHDF1 and marker channel. Scale bar 20 μm. **d.** Quantification of immunoreactivity showing significantly higher YTHDF1 expression in neurons. **e.** Confocal images showing DIV4 dissociated hippocampal neurons expressing cell-filler EGFP (green) stained with YTHDF1 (magenta). Scale bar 20 μm. Inset images showing YTHDF1 staining in **e1** soma, **e2** dendrite, **e3** axon and **e4** axonal growth cone.

Figure 2. YTHDF1 is required for post-mitotic development of neurons in culture

a. Schematic representation of knockdown strategy at different stages of neuronal development encompassing polarization, axonal and dendritic development, spinogenesis, and spine maturation. **b.** Fluorescence images showing DIV4 dissociated hippocampal culture neurons expressing shCtrl and shYTHDF1 along with EGFP (inset) stained with DAPI (blue), Phalloidin (red), Glu-Tubulin (green). Numbers denoting the percentage of dominant axons (green) and percentage of neurites bearing prominent actin caps at the tip (red). n=neurons analyzed per group. Scale bar 10 μm **c.** Graphic representations of DIV6 neurons expressing shCtrl / shYTHDF1 with EGFP. Scale bar 50 μm. **d.** Group quantification of the longest axonal branch length (n=number of neurons analyzed). **e.** Group quantification of the total number of axonal branch tips (n=number of neurons analyzed). **f.** Confocal images of DIV7 neurons, expressing EGFP, shCtrl / shYTHDF1, stained with DAPI (blue) and YTHDF1 (magenta). Insets: YTHDF1 immunostaining in soma. Scale bar 20 μm. **g.** Line plots comparing the dendritic Sholl profiles between control and YTHDF1-KD neurons. **h.** Confocal images of DIV12 neurons expressing EGFP with shCtrl / shYTHDF1. Scale bar 20 μm. Insets: dendritic shafts magnified to visualize dendritic spines. Scale bar 5 μm. **i.** Group spine classification in DIV12 shCtrl (C) and shYTHDF1 (KD) dendrites . **j.** Group quantification of spine density (per 10 μm) between DIV12 C and KD (n=dendritic shafts analyzed). **k.** Confocal images of DIV18 neurons expressing EGFP with shCtrl / shYTHDF1. Scale bar 20 μm. Insets: dendritic shafts magnified to visualize dendritic spines. Scale bar 5 μm. **l.** Group spine classification in DIV18 C and KD. **m.** Group quantification of spine density (per 10 μm) between DIV18 C and KD (n=dendritic shafts analyzed).

Figure 3. Knocking down YTHDF1 hampers early postnatal development of hippocampal DG neurons *in vivo*

a. DNA constructs for CRE-inducible shRNA vectors. nCRE or ER^{T2}-CRE-ER^{T2}, EGFP, and pCALSL-miR30 expression vector (containing shRNA, with upstream transcription stop signal flanked by lox P sites) were mixed for *in-vivo* electroporation (IVE). **b.** The experimental scheme of IVE (P0), CRE-induction (TAM, P17-19), and brain tissue collection at P7 or P23 for imaging and analysis. **c.** Representative confocal images showing a P7 hippocampal slice stained with DAPI (blue). GFP+ cells represent those with expression of the electroporated plasmids at P0. Note much less GFP+ cells are found in dentate gyrus (DG) and Tertiary dentate matrix (TDM) of shYTHDF1 animals. Scale bar 200 μm. **d.** Group quantification of the migrated neurons in the granule cell layer (GCL) and TDM region of DG (median number of migrated neurons per section in GCL: shCtrl 7.94±5.79, shYTHDF1 4.98±4.05 neurons; TDM: shCtrl 6.55±3.83, shYTHDF1 5.09±3.34 neurons). **e.** Representative confocal images of P23 single DG granule neurons. Insets show enlarged dendrites populated with dendritic spines. Scale bar: whole cell images 15 μm; insets 2 μm. **f.** Line plots comparing the dendritic 3D-Sholl profiles between control and YTHDF1-KD neurons. **g.** Schematic illustration showing segmentation and mathematical parameters for arborization morphometric analysis. Colored sticks represent depth or level of dendritic segments. Colored dots represent branching and tip points. This information was used by Imaris to quantify the arborization pattern and properties of each individual dendrite. **h.** Branch level plotted as a function of branch depth showing disordered branching in YTHDF1-KD. **i.** straightness along branch depth showing less straight dendrites of YTHDF1-KD

neurons. **j.** Cumulative branch depth showing less branching in YTHDF1-KD neurons. **k.** Cumulative branching angels show “wider” branching angles in YTHDF1-KD. **l.** Schematic illustration showing segmentation and mathematical parameters for dendritic morphological analysis. **m.** Cumulative dendritic length showing reduction in YTHDF1-KD (L1+L2); **n.** Cumulative mean diameter (d1+d2+d3)/3) showing “thinner” dendrites in YTHDF1-KD; **o.** Cumulative surface showing “thinner” dendrites in YTHDF1-KD. **p.** Cumulative volume showing “smaller” dendrites in YTHDF1-KD. **q.** Representative rendered images of dendrite fragments (yellow) and spines (cyan) in shCtrl and shYTHDF1 neurons; **r.** Cumulative spine volume showing “smaller” spines in the outer layer of DG receiving input from LEC. **s.** Cumulative spine volume showing “smaller” spines in the middle layer of DG receiving input from MEC. **t.** Group quantification of spine volume showing significant reduction in shYTHDF1-KD neurons. **u.** Group quantification of spine density showing significant reduction in shYTHDF1-KD neurons.

Figure 4. Developmentally regulated APC-RNA granule at the plus-end of the microtubule is enriched with m^6A and associated with YTHDF1

a. Bar graph showing the percentage of overlapping m^6A modified mRNA species in each interacting RNA dataset. A broken line is drawn as up to 50% of mRNA are estimated as m^6A modified in brain. **b.** Hypergeometric analysis showing 187 APC-bound mRNA (E14 mice) intersected with m^6A-mRNA database, a significant enrichment (11655 RNAs expressed in the embryonic mouse brain were used as background)[45,48] **c.** Pie chart showing topological distribution of peaks along the APC-bound m^6A transcripts. **d.** m^6A dot-blot of poly(A) RNA purified from tissue

homogenate (Input), APC immunoprecipitate (IP), IgG immunoprecipitated (IgG). Equal amount of RNA (4% of the total input, 9% of APC-IPed) RNA was blotted. Equal amount of an *in vitro* transcribed RNA containing no RNA modification was used as negative control. **e.** Heatmap showing z score of expression values (TPM) for 274 APC-bound RNAs as well as Apc RNA in three developmental stages of the mouse (E13, P14, and adult). **f.** Left two columns, log2FC of methylation scores of 1,921 DMs; right two columns, log2FC of corresponding mRNA expression; in respective developmental timepoints. The log2FC values are sorted in ascending order from right to left ("NA": non-differential). Black: not differential. **g.** Representative mapped read coverage images of developmentally regulated m^6A loci in Tbr1, Ctnnb1, and Tubb2b genes. **h.** Representative Western-blots showing m^6A reader, writer, and eraser proteins in tissue homogenate (input), IgG immunoprecipitated (IgG), and APC immunoprecipitated (APC). **i.** Representative Western-blots showing YTHDF1 along with translation initiation factors and ribosomal protein in input, APC IP, IgG control samples with or without RNAse A treatment. **j.** Top: super-resolution fluorescence images of axonal growth cone (DIV6) and dendrite with spines (DIV18) stained with APC (green) and YTHDF1 (red). In the axonal growth cone panel, left: acquired image; middle: reconstructed image detecting fluorescence puncta; right: reconstructed image with APC puncta rendered to 600 nm. In the dendritic spine panel top: acquired image, dendritic shaft contour is denoted by white border created through EGFP masking; bottom left: reconstructed image detecting fluorescence puncta; bottom right: reconstructed image with APC puncta rendered to 600 nm. Numbers denote the percentage of APC puncta co-localizing with YTHDF1 puncta. Scale bar 5 μm.

Figure 5. Knocking down m^{6}A writer METTL14 or APC caseud neuronal phenotypes resembling YTHDF1-KD

a. Schematic diagram depicting m^{6}A-YTHDF1-APC complex at the dynamic end of neuronal microtubule, and genetic manipulation strategies to perturb the epitranscriptomic control of APC granules or the expression of APC itself using shRNAs and overexpression. **b.** Graphic representations of DIV6 neurons expressing shCtrl (n=14-17) / shMETTL14 (sh1: n=16, sh2: n=18) / shYTHDF1 (sh1: n=13, sh2: n=27) / shAPC (sh2: n=16, sh3: n=17) / empty vector (n=16) / FTO (n=16) along with EGFP, n= neurons analyzed. Axonal branch tips are highlighted. Scale bar 50 μm. **c.** Group quantifications of the length of longest axon normalized to Ctrl. **d.** Group quantifications of total number of axonal branch tips normalized to Ctrl. **e.** Confocal images of DIV7 neurons expressing shCtrl (n=14-20) / shMETTL14 (sh1: n=18, sh2: n=16) / shYTHDF1 (sh1: n=20, sh2: n=18)/ shAPC (sh2: n=16, sh3: n=17)/ empty vector (n=16) / FTO (n=16) along with EGFP, stained with DAPI (blue), n= neurons analyzed. Scale bar 20 μm. **f.** Group quantifications of the enclosing radius of dendritic arbor normalized to Ctrl. **g.** Group quantifications of the sum intersections in shMETTL14 / shYTHDF1 / shAPC / FTO cells normalized to Ctrl.

Figure 6. METTL14 and YTHDF1 are required for APC-RNA granule expression and microtubule function

a. Representative confocal images showing DIV 7 neurons expressing EGFP with shCtrl / shMETTL14 / shYTHDF1 stained with APC. Scale bars: 20 μm. Insets: super-resolution imaging showing APC granules in dendrites. Scale bars: 5 μm. The

contour of the EGFP masked neurons and dendrites have been defined by white borders. **b.** Group quantification of the fluorescence intensity of APC granules in dendrites (n=APC granules analyzed). **c.** Representative confocal images showing DIV7 neurons expressing EGFP with shCtrl / shMETTL14 / shYTHDF1 stained with β-tubulin 2b (TUBB2B), Tyrosinated Tubulin (Tyr-TUB) and MAP2. Scale bar 10 μm. The contour of the EGFP masked neurons have been defined by white borders. **d.** Group quantifications of the fluorescence intensity of TUBB2B, Tyr-TUB and MAP2 (n=number of neurons analyzed). **e.** Representative confocal images showing DIV7 neurons expressing EB3-GFP with shCtrl / shMETTL14 / shYTHDF1. White arrows pointing to "debundling" in primary dendrite. Scale bar 5 μm. **f.** Confocal images in grayscale showing two broadly categorized axonal growth cone phenotypes: intact and collapsed. Blue borders surrounding the growth cones denoting the growth cone area. Confocal images showing axonal growth cone phenotypes from DIV6 neurons expressing shCtrl / shMETTL14 / shYTHDF1/ shAPC along with EGFP. Scale bar 5 μm. **g.** Percentage of intact and collapsed growth cones in control and KD groups. numbers=growth cones analyzed. **h.** Group quantification of growth cone area (shCtrl: n=41; shYTHDF1-1: n=20; shYTHDF1-2: n=21; shAPC-2: n=16; shAPC-3: n=28; shMETTL14-1: n=20; shMETTL14-2: n=22; n=growth cones analyzed).

Figure 7. Autism and Schizophrenia-associated mutations in METTL14 impact APC expression and neuron development

a. The overview structure of the human METTL3/METTL14 core complex (PDB code: 5il0). I311 and p-S399 are shown in squares. S-adenosylmethionine (SAM) is superimposed. **b.** Model structures of I311V and S399L mutations introduced by

PyMOL are simulated. Interacting residues are identified by Ligplot and depicted. **c.** Representative confocal images showing DIV7 neurons expressing EGFP with Empty pCAGGS / OE METTL14 WT / OE METTL14 I311V / OE METTL14 S399L stained with APC (magenta). Scale bars 20 µm. Insets: super-resolution imaging showing APC granules in the selected dendritic shafts. Scale bar 5 µm. The contour of the EGFP masked neurons and dendrites have been defined by white borders. **d.** Line plot comparing the median dendritic sholl profiles between Empty, METTL14 WT, METTL14 I311V, METTL14 S399L neurons, X and Y axis is denoting the distance from the soma (µm) and the number of intersections ± SEM respectively **e.** Group quantification of the fluorescence intensity of APC in soma (Empty: n=40; METTL14 WT: n=48; METTL14 I311V: n=75; METTL14 S399L: n=71; n=cells analyzed,). **f.** Group quantification of the fluorescence intensity of APC granules (Number of APC granules analyzed : Empty n=667; METTL14 WT n=411; METTL14 I311V n=220; METTL14 S399L n=220). **g.** Confocal images showing axonal growth cone phenotypes from DIV6 neurons expressing Empty / METTL14 WT / METTL14 I311V / METTL14 S399L along with EGFP. Scale bar 5 µm. **h.** Group quantification of growth cone area (Number of growth cones analyzed, Empty n=15; METTL14 WT n=14; METTL14 I311V n=14; METTL14 S399L n=14). **i.** Confocal images of DIV7 neurons expressing Empty / METTL14 WT / METTL14 I311V / METTL14 S399L along with EGFP, stained with Tyrosinated (Tyr) Tubulin (magenta) and MAP2 (yellow). Scale bar 5 µm. The contour of the EGFP masked neurons have been defined by white borders. **j-k.** Group quantifications of the fluorescent intensity of Tyr-Tubulin and MAP2 (Number of cells analyzed, Empty Tyr-Tub n=19; METTL14 WT Tyr-Tub n=17; METTL14 I311V Tyr-Tub n=17; METTL14

S399L Tyr-Tub n=16; Empty MAP2 n=19; METTL14 WT MAP2 n=17; METTL14 I311V MAP2 n=17; METTL14 S399L MAP2 n= 16). **l.** Confocal images of DIV7 neurons, expressing shCtrl Empty / shCtrl METTL14-WT / shMETTL14 Empty / shMETTL14 METTL14-WT / shMETTL14 METTL14-I311V / shMETTL14 METTL14-S399L along with EGFP, stained with DAPI (blue) and METTL14 (magenta). Inset is showing METTL14 immunoreactivity in control and METTL14 KD and rescued neurons. Scale bar 20 µm. **m.** Line plot comparing the median dendritic sholl profiles between shCtrl-Empty, shCtrl-METTL14(WT), shCtrl-METTL14(I311V), shCtrl-METTL14(S399L), shMETTL14-Empty, shMETTL14-METTL14(WT), shMETTL14-METTL14(I311V), shMETTL14-METTL14(S399L) neurons, X and Y axis is denoting the distance from the soma (µm) and the number of intersections ± SEM respectively. **n.** Group quantifications of the fluorescent intensity of APC (Number of neurons analyzed; shCtrl-Empty n=42, shMETTL14-Empty n=34, shMETTL14-METTL14(WT) n=31, shMETTL14-METTL14(I311V) n=42, shMETTL14-METTL14(S399L) n=53) .

Supplementary Figure S1: YTHDF1 is a neuronal m^{6}A reader widely expressed in mouse brain

a. t-distributed stochastic neighbor embedding (tSNE) plot showing neurons (red), glia (green) and ependymal (blue) populations identified from adult mouse hippocampal single cell RNA-seq (scRNA-seq) dataset. **b.** tSNE plots showing the mRNA expression of m^{6}A readers *Ythdf1*, *Ythdf2*, *Ythdf3* across above identified cell type clusters. **c.** tSNE plot showing clusters of different glial subpopulations including Oligodendrocytes (ODC), Microglia, Oligodendrocyte Progenitor Cells (OPC), Astrocytes identified from the adult mouse hippocampal single cell RNA-seq (scRNA-seq) dataset. **d.** Violin plots

showing the expression of m^6A readers Ythdf1, Ythdf2, Ythdf3 in different glial subpopulations. **e.** Fluorescence image of the whole brain section (same as Fig 1) showing colocalization between YTHDF1 and NeuN in the different brain regions, denoted by different color coded boxes. Scale bar 500 μm. Magnified images showing the colocalization of YTHDF1 and NeuN in different cortical layers, cerebellum, Thalamus, DG of hippocampus, Hypothalamus. Scale bar 50 μm. **f.** Fluorescence images of DIV13 dissociated hippocampal culture mixed with neuron and glia immunostained with YTHDF1 (red), along with DAPI (blue) and different cell type markers (green): NeuN, GFAP, CamKII, GAD67, MBP, Iba1. Arrows pointing to different cell types. Scale bar 20 μm. **g.** Quantification of immunoreactivity showing significantly higher YTHDF1 expression in neurons.

Supplementary Figure S2: YTHDF1 is required for post-mitotic development of neurons in culture

a. Group quantification of YTHDF1 intensity after YTHDF1-KD during axonal and dendritic development (n=neurons analyzed). **b.** Group quantification of the number of primary neurites at DIV 4 after shRNA mediated YTHDF1-KD (n=neurons analyzed) **c.** Group quantification of the morphometric analysis related to dendritic development after YTHDF1-KD (n=neurons analyzed). **d.** Superresolution imaging showing YTHDF1 immunoreactivity (red) as puncta in dendritic shafts and dendritic spines during dendritic development (DIV7), spinogenesis initiation (DIV11), and spine maturation (DIV18) in the dissociated hippocampal culture neurons expressing EGFP. In the right panel contour of the dendrites and dendritic spines was traced through EGFP expression. Scale bar 5 μm. **e.** Line plots comparing the dendritic Sholl profiles between shCtrl and

shYTHDF1 (related to Fig. 2k) **f.** Group quantification of sum intersections between DIV18 shCtrl and shYTHDF1 (n=neurons analyzed). **g.** Group quantification of enclosing radius between DIV18 shCtrl and shYTHDF1 (n=neurons analyzed).

Supplementary figure S3: Knocking down YTHDF1 hampers early postnatal development of hippocampal DG neurons *in vivo*

a. Representative confocal images of YTHDF1 immunostaining (magenta) in P7 DG. top row: GFP+ signals label shCtrl / shYTHDF1-1 / shYTHDF1-2 cells; middle row: YTHDF1 immunoreactivity in DG; Insets (bottom row): magnified GFP masked neurons showing YTHDF1 immunoreactivity. Scale bars: 12.23 μm. **b.** Group quantification of YTHDF1 intensity in GFP+ cells. Intensity is measured in soma and proximal dendrite. **c.** Annotated hippocampal slices in IVE animals. The fluorescence image shows the distribution of the IVE neurons (GFP+, green) in hippocampus formation stained with YTHDF1 (purple) at P7 (left) and P23 (right) in the shCtrl group. The black arrow represents the migratory pathway of DG cells from the fimbrial along the suprafimbrial path to TDM and DG. At P23, migrated DG neurons have developed dendrites that reach the molecular layer. SDM: secondary dentate matrix; NC: neocortex; TDM: tertiary dentate matrix; DG: dentate gyrus; CA: cornus ammonis.

Supplementary Figure S4: Knocking down YTHDF1 hampers early postnatal development of hippocampal DG neurons *in vivo*

Representative confocal images showing the overall morphology of P23 granule cells in the DG expressing shCtrl (upper panel) and shYTHDF1 (lower panel) along with EGFP. Scale bar 50 μm.

Supplementary Figure S5: Developmentally regulated APC-RNA granule at the plus-end of the microtubule is enriched with m^6A and associated with YTHDF1

a. Quantification of the dot intensity in Fig. 4d. **b.** poly(A) concentrations in Input and APC IP'ed total RNA were measured as relative fluorescence unit (RFU) values of ECHO probes against poly(A) upon hybridization. Poly(A) RNA purified from the mouse brain total RNA and poly(A) salt used as positive control. RFU values obtained from ECHO probe used as background signal.

Supplementary figure S6 : Knocking down m^6A writer METTL14 or APC caseud neuronal phenotypes resembling YTHDF1-KD

a. Group quantification of METTL14 immunostaining intensity after METTL14-KD during axonal and dendritic development (n=neurons analyzed). **b.** Group quantification of APC intensity after APC-KD during axonal and dendritic development (n=neurons analyzed). **c-e.** Line plots comparing the dendritic Sholl profiles between shCtrl and shMETTL14 / shDF1-KD / shAPC-KD neurons respectively (related to Fig. 5e). **f-h.** Group quantification of the length of the dendritic arbor after shRNA mediated METTL14-KD / YTHDF1-KD / APC-KD respectively during dendritic development (related to Fig. 5e and 5f) (n=neurons analyzed). **i-k.** Group quantification of sum intersections in shCtrl / METTL14-KD / YTHDF1-KD / APC-KD for dendritic development (related to Fig. 5e and 5g) (n=neurons analyzed).

Supplementary figure S7 : METTL14 and YTHDF1 are required for APC-RNA granule expression and microtubule function

a. Confocal images of DIV7 neurons, expressing Empty / pCAGGS-HA-FTO along with EGFP, stained with DAPI (blue), APC (magenta) and HA (red). Insets: APC immunoreactivity in control and FTO overexpressed (OE) neurons. Scale bar 20 µm. **b.** Group quantification of HA immunostaining intensity (A.U.) in FTO OE (n=neurons analyzed) **c.** Group quantification of APC immunostaining intensity (A.U.) after FTO OE (n=number of neurons analyzed). **d.** Venn diagram showing the overlap between the hypermethylated genes in FTO KO animals and APC target genes.

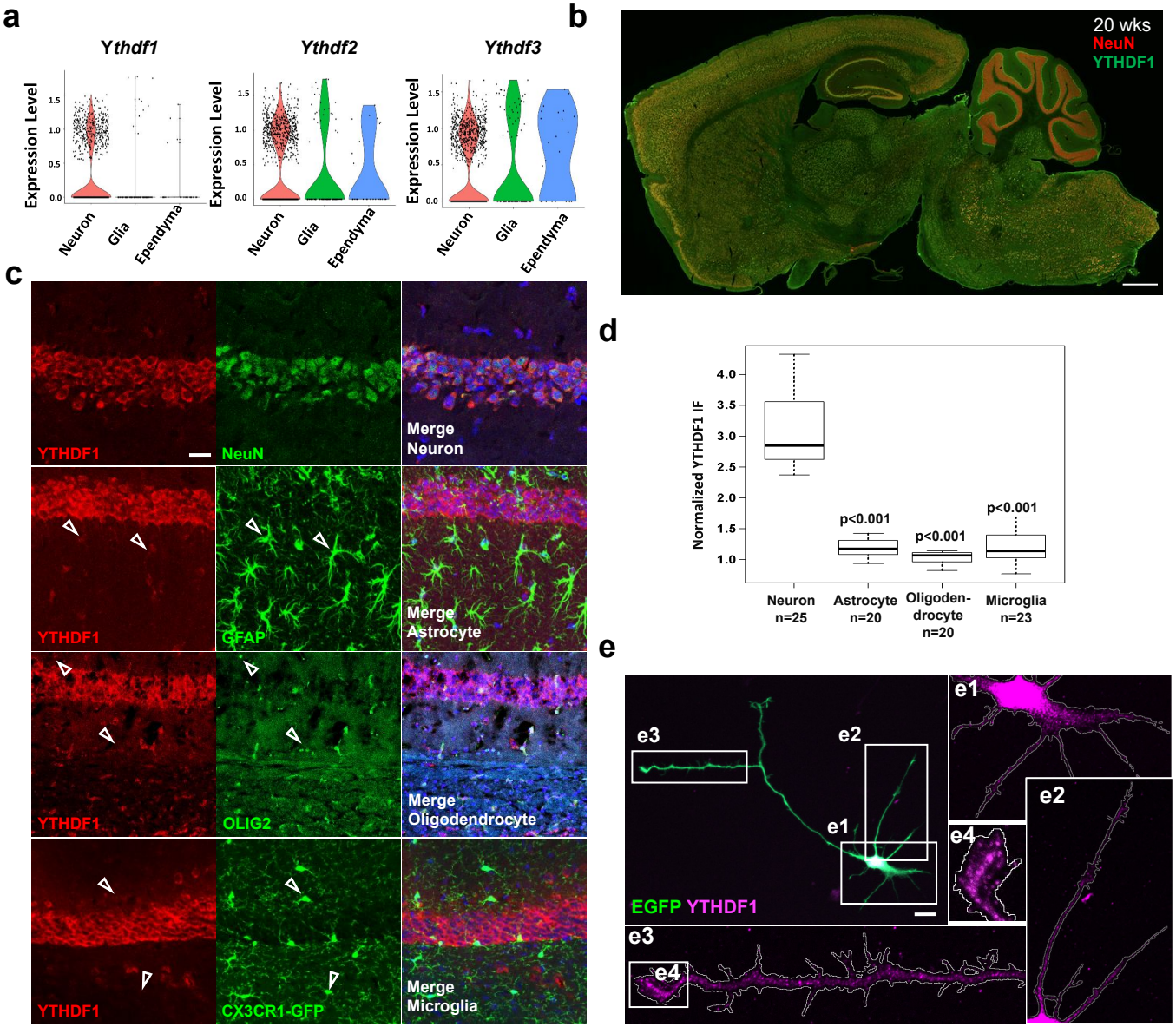
a
Ythdf1
Ythdf2
Ythdf3
Expression Level
Neuron
Glia
Ependyma
b
20 wks
NeuN
YTHDF1
c
YTHDF1
NeuN
Merge
Neuron
GFAP
Merge
Astrocyte
OLIG2
Merge
Oligodendrocyte
CX3CR1-GFP
Merge
Microglia
d
Normalized YTHDF1 IF
p<0.001
Neuron
n=25
Astrocyte
n=20
Oligoden-
drocyte
n=20
Microglia
n=23
e
e1
e2
e3
e4
EGFP YTHDF1

Figure 1

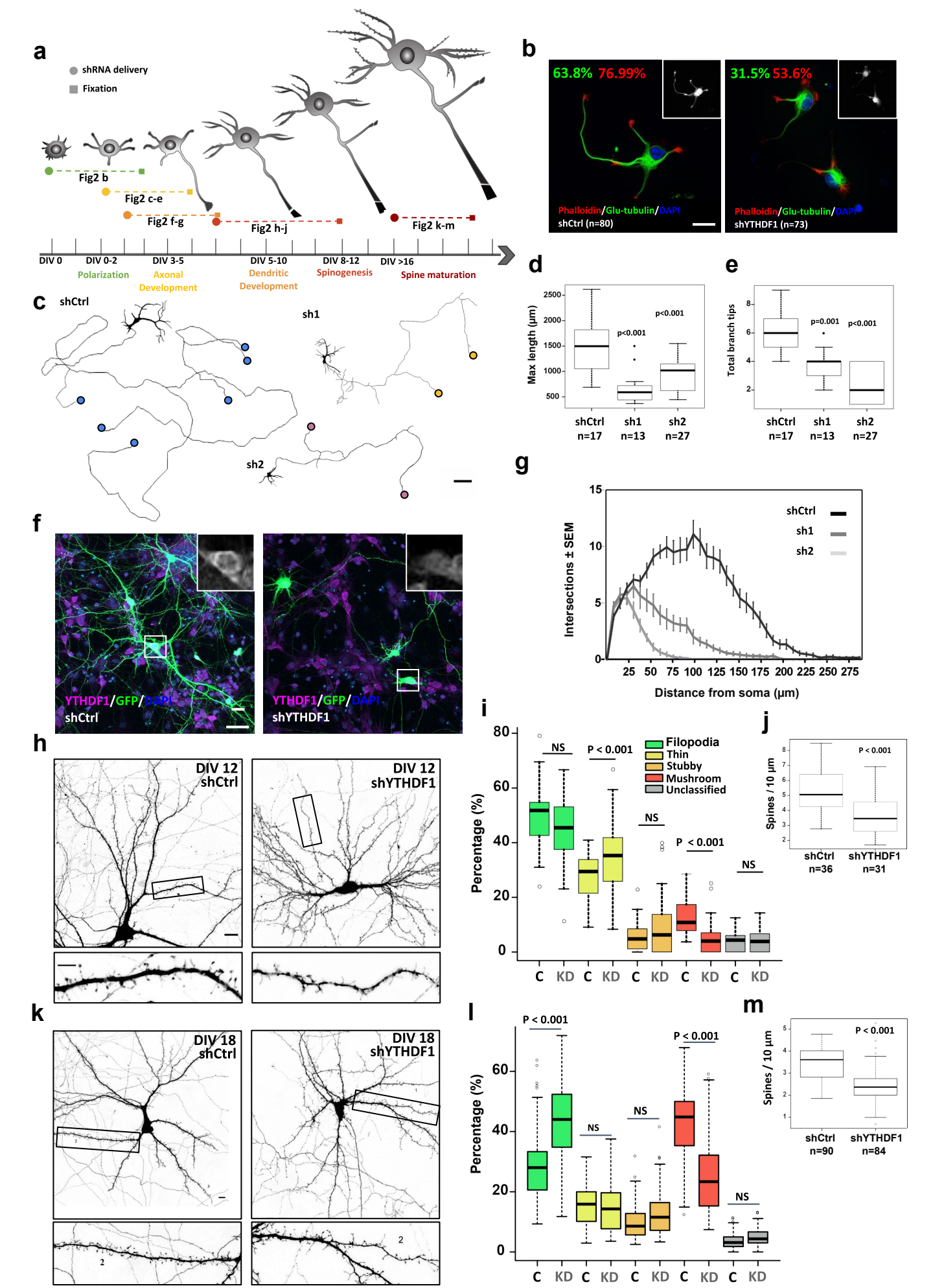
a
shRNA delivery
Fixation
Fig2 b
Fig2 c-e
Fig2 f-g
Fig2 h-j
Fig2 k-m
DIV 0
DIV 0-2
Polarization
DIV 3-5
Axonal Development
DIV 5-10
Dendritic Development
DIV 8-12
Spinogenesis
DIV >16
Spine maturation
b
63.8% 76.99%
Phalloidin/Glu-tubulin/DAPI
shCtrl (n=80)
31.5% 53.6%
Phalloidin/Glu-tubulin/DAPI
shYTHDF1 (n=73)
c
shCtrl
sh1
sh2
d
Max length (µm)
p<0.001
p<0.001
shCtrl n=17
sh1 n=13
sh2 n=27
e
Total branch tips
p=0.001
p<0.001
shCtrl n=17
sh1 n=13
sh2 n=27
f
YTHDF1/GFP/DAPI
shCtrl
YTHDF1/GFP/DAPI
shYTHDF1
g
Intersections ± SEM
shCtrl
sh1
sh2
Distance from soma (µm)
h
DIV 12 shCtrl
DIV 12 shYTHDF1
i
Percentage (%)
NS
P < 0.001
NS
P < 0.001
NS
Filopodia
Thin
Stubby
Mushroom
Unclassified
C KD C KD C KD C KD C KD
j
Spines / 10 µm
P < 0.001
shCtrl n=36
shYTHDF1 n=31
k
DIV 18 shCtrl
DIV 18 shYTHDF1
l
Percentage (%)
P < 0.001
NS
NS
P < 0.001
NS
C KD C KD C KD C KD C KD
m
Spines / 10 µm
P < 0.001
shCtrl n=90
shYTHDF1 n=84

Figure 2

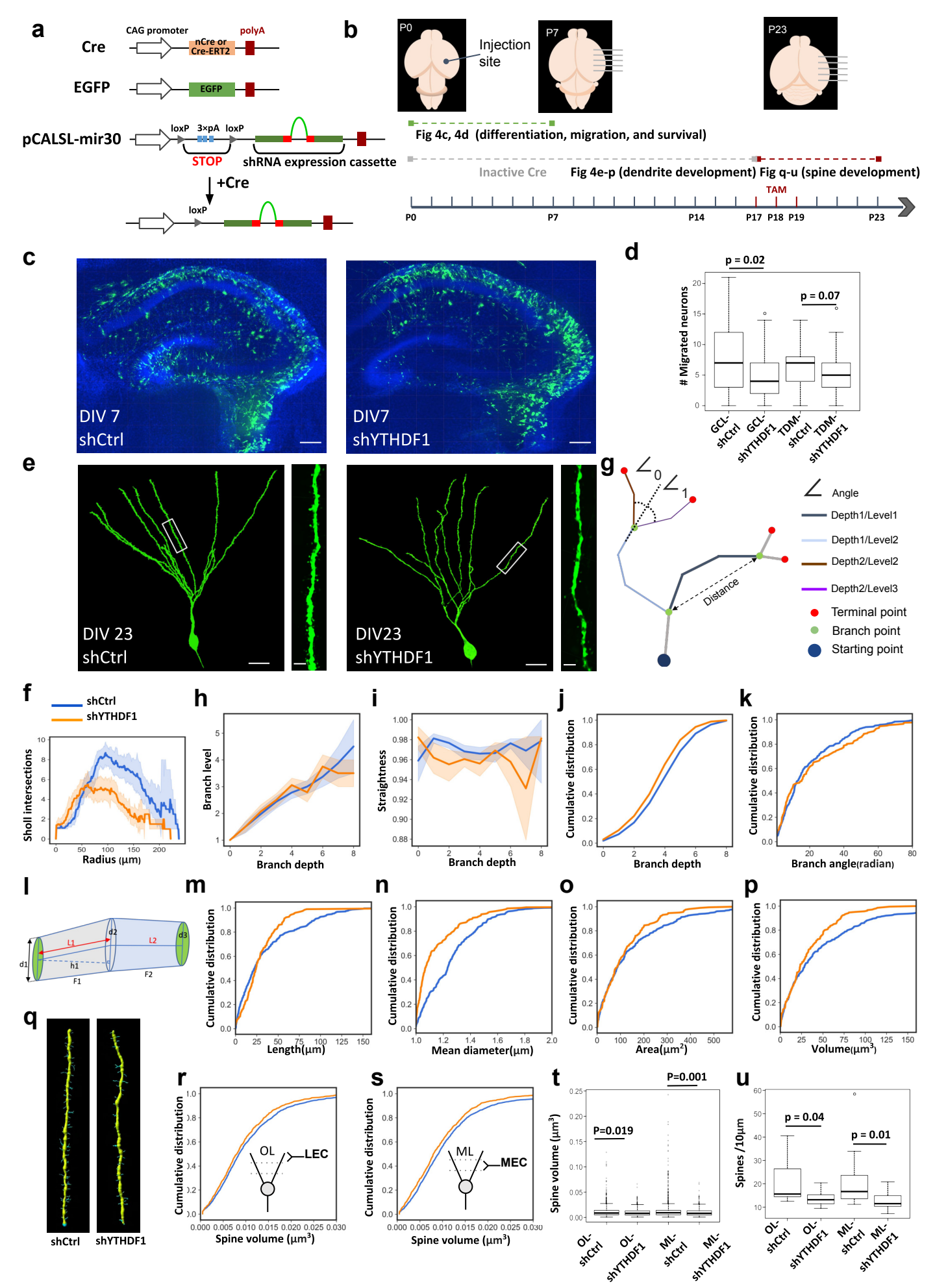
a
Cre
CAG promoter
nCre or Cre-ERT2
polyA
EGFP
EGFP
pCALSL-mir30
loxP
3×pA
loxP
STOP
shRNA expression cassette
+Cre
loxP
b
P0
Injection site
P7
P23
Fig 4c, 4d (differentiation, migration, and survival)
Inactive Cre
Fig 4e-p (dendrite development) Fig q-u (spine development)
TAM
P0
P7
P14
P17
P18
P19
P23
c
DIV 7
shCtrl
DIV7
shYTHDF1
d
p = 0.02
p = 0.07
# Migrated neurons
GCL-shCtrl
GCL-shYTHDF1
TDM-shCtrl
TDM-shYTHDF1
e
DIV 23
shCtrl
DIV23
shYTHDF1
g
Angle
Depth1/Level1
Depth1/Level2
Depth2/Level2
Depth2/Level3
Terminal point
Branch point
Starting point
Distance
f
shCtrl
shYTHDF1
Sholl intersections
Radius (μm)
h
Branch level
Branch depth
i
Straightness
Branch depth
j
Cumulative distribution
Branch depth
k
Cumulative distribution
Branch angle(radian)
l
L1
L2
d1
d2
d3
h1
F1
F2
m
Cumulative distribution
Length(μm)
n
Cumulative distribution
Mean diameter(μm)
o
Cumulative distribution
Area(μm²)
p
Cumulative distribution
Volume(μm³)
q
shCtrl
shYTHDF1
r
Cumulative distribution
OL
LEC
Spine volume (μm³)
s
Cumulative distribution
ML
MEC
Spine volume (μm³)
t
P=0.001
P=0.019
Spine volume (μm³)
OL-shCtrl
OL-shYTHDF1
ML-shCtrl
ML-shYTHDF1
u
p = 0.04
p = 0.01
Spines /10μm
OL-shCtrl
OL-shYTHDF1
ML-shCtrl
ML-shYTHDF1

Figure 3

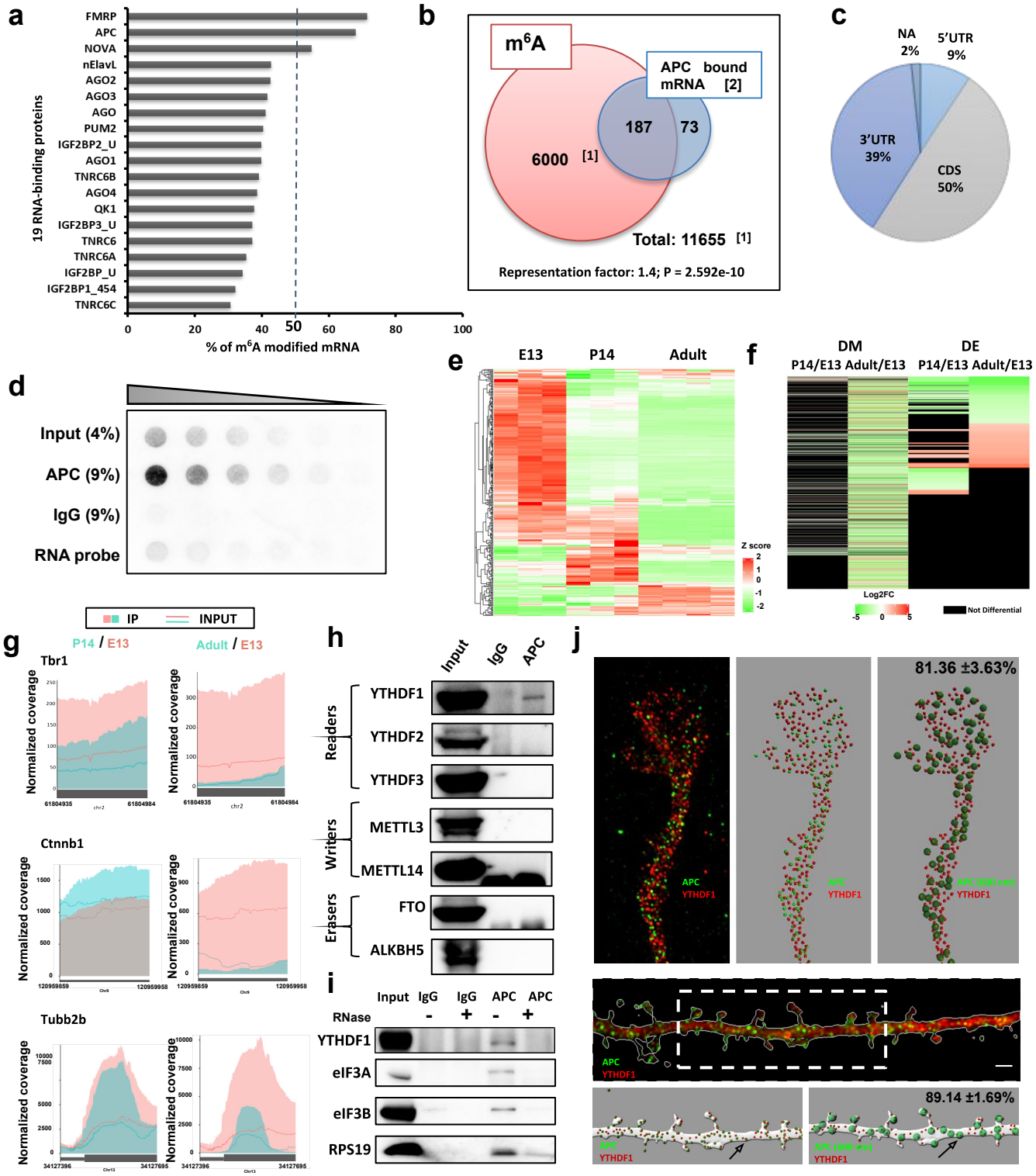
a
FMRP
APC
NOVA
nElavL
AGO2
AGO3
AGO
PUM2
IGF2BP2_U
AGO1
TNRC6B
AGO4
QK1
IGF2BP3_U
TNRC6
TNRC6A
IGF2BP_U
IGF2BP1_454
TNRC6C
19 RNA-binding proteins
0
20
40
50
60
80
100
% of m6A modified mRNA
b
m6A
APC bound mRNA [2]
187
73
6000 [1]
Total: 11655 [1]
Representation factor: 1.4; P = 2.592e-10
c
NA 2%
5'UTR 9%
3'UTR 39%
CDS 50%
d
Input (4%)
APC (9%)
IgG (9%)
RNA probe
e
E13
P14
Adult
Z score
f
DM
P14/E13 Adult/E13
DE
P14/E13 Adult/E13
Log2FC
Not Differential
g
IP
INPUT
P14 / E13
Adult / E13
Tbr1
Ctnnb1
Tubb2b
Normalized coverage
h
Input
IgG
APC
Readers
YTHDF1
YTHDF2
YTHDF3
Writers
METTL3
METTL14
Erasers
FTO
ALKBH5
i
Input
IgG
IgG
APC
APC
RNase
-
+
-
+
YTHDF1
eIF3A
eIF3B
RPS19
j
81.36 ±3.63%
APC
YTHDF1
APC (600 nm)
YTHDF1
89.14 ±1.69%

Figure 4

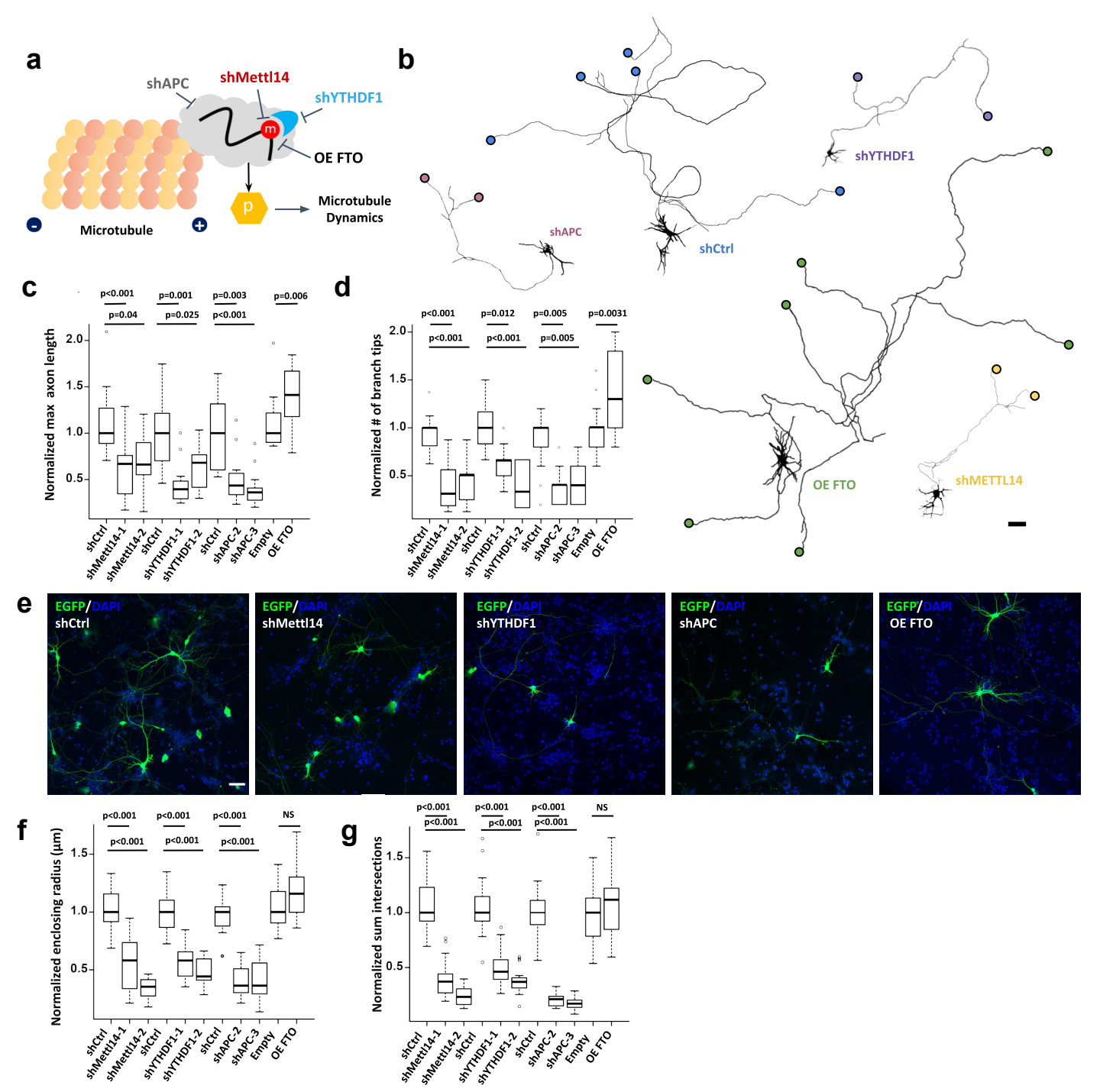
a
shAPC
shMettl14
shYTHDF1
m
OE FTO
p
Microtubule Dynamics
Microtubule
b
shYTHDF1
shAPC
shCtrl
OE FTO
shMETTL14
c
Normalized max axon length
p<0.001
p=0.04
p=0.001
p=0.025
p=0.003
p<0.001
p=0.006
shCtrl
shMettl14-1
shMettl14-2
shCtrl
shYTHDF1-1
shYTHDF1-2
shCtrl
shAPC-2
shAPC-3
Empty
OE FTO
d
Normalized # of branch tips
p<0.001
p<0.001
p=0.012
p<0.001
p=0.005
p=0.005
p=0.0031
e
EGFP/DAPI
shCtrl
shMettl14
shYTHDF1
shAPC
OE FTO
f
Normalized enclosing radius (µm)
p<0.001
p<0.001
p<0.001
p<0.001
p<0.001
p<0.001
NS
g
Normalized sum intersections
p<0.001
p<0.001
p<0.001
p<0.001
p<0.001
p<0.001
NS

Figure 5

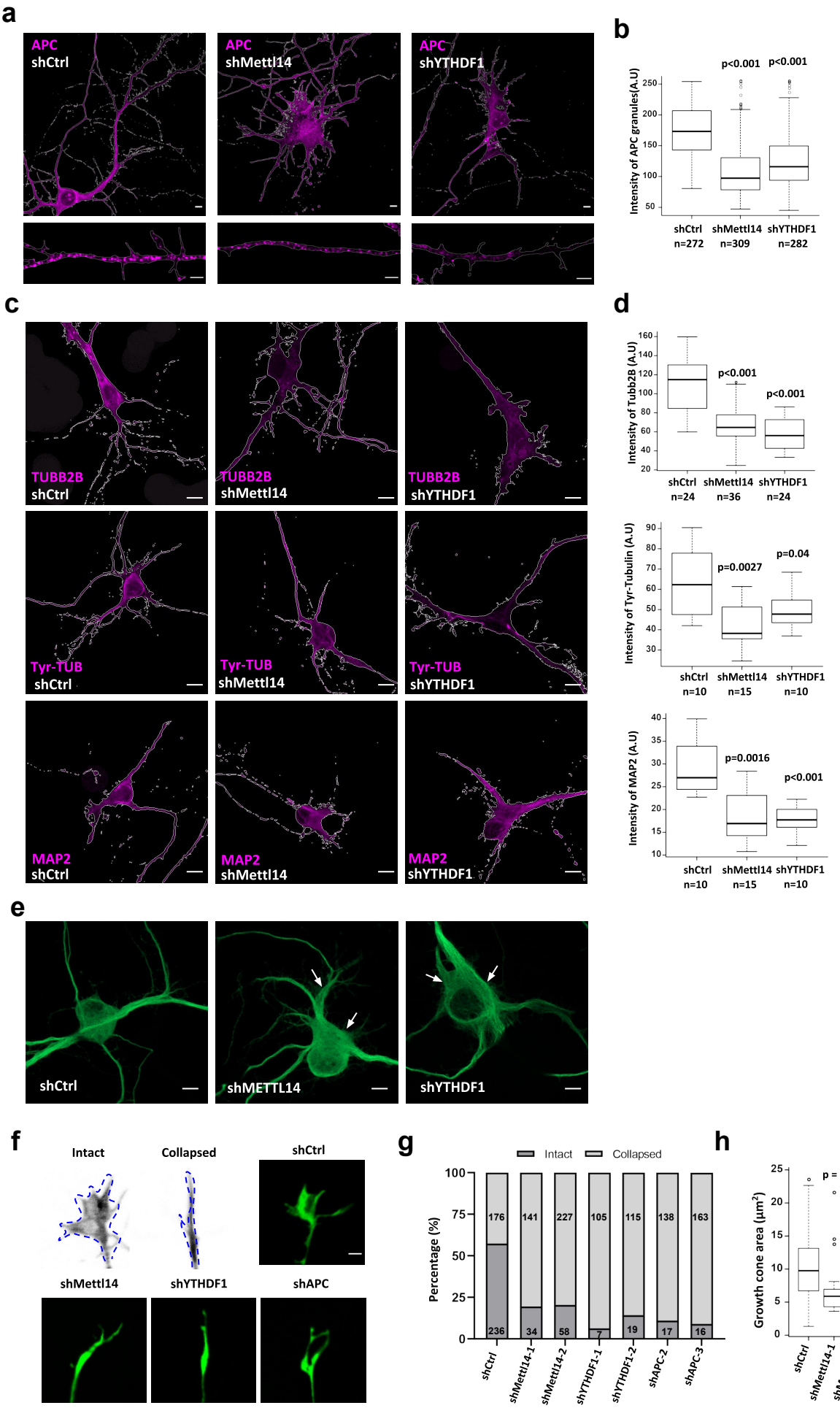
a
APC
shCtrl
APC
shMettl14
APC
shYTHDF1
b
p<0.001
p<0.001
Intensity of APC granules(A.U)
shCtrl
n=272
shMettl14
n=309
shYTHDF1
n=282
c
TUBB2B
shCtrl
TUBB2B
shMettl14
TUBB2B
shYTHDF1
Tyr-TUB
shCtrl
Tyr-TUB
shMettl14
Tyr-TUB
shYTHDF1
MAP2
shCtrl
MAP2
shMettl14
MAP2
shYTHDF1
d
Intensity of Tubb2B (A.U)
p<0.001
p<0.001
shCtrl
n=24
shMettl14
n=36
shYTHDF1
n=24
Intensity of Tyr-Tubulin (A.U)
p=0.0027
p=0.04
shCtrl
n=10
shMettl14
n=15
shYTHDF1
n=10
Intensity of MAP2 (A.U)
p=0.0016
p<0.001
shCtrl
n=10
shMettl14
n=15
shYTHDF1
n=10
e
shCtrl
shMETTL14
shYTHDF1
f
Intact
Collapsed
shCtrl
shMettl14
shYTHDF1
shAPC
g
Intact
Collapsed
Percentage (%)
176
141
227
105
115
138
163
236
34
58
7
19
17
16
shCtrl
shMettl14-1
shMettl14-2
shYTHDF1-1
shYTHDF1-2
shAPC-2
shAPC-3
h
Growth cone area (μm²)
p = 0.01
p < 0.001
p < 0.001
p < 0.001
p < 0.001
p = 0.01
shCtrl
shMettl14-1
shMettl14-2
shYTHDF1-1
shYTHDF1-2
shAPC-2
shAPC-3

Figure 6

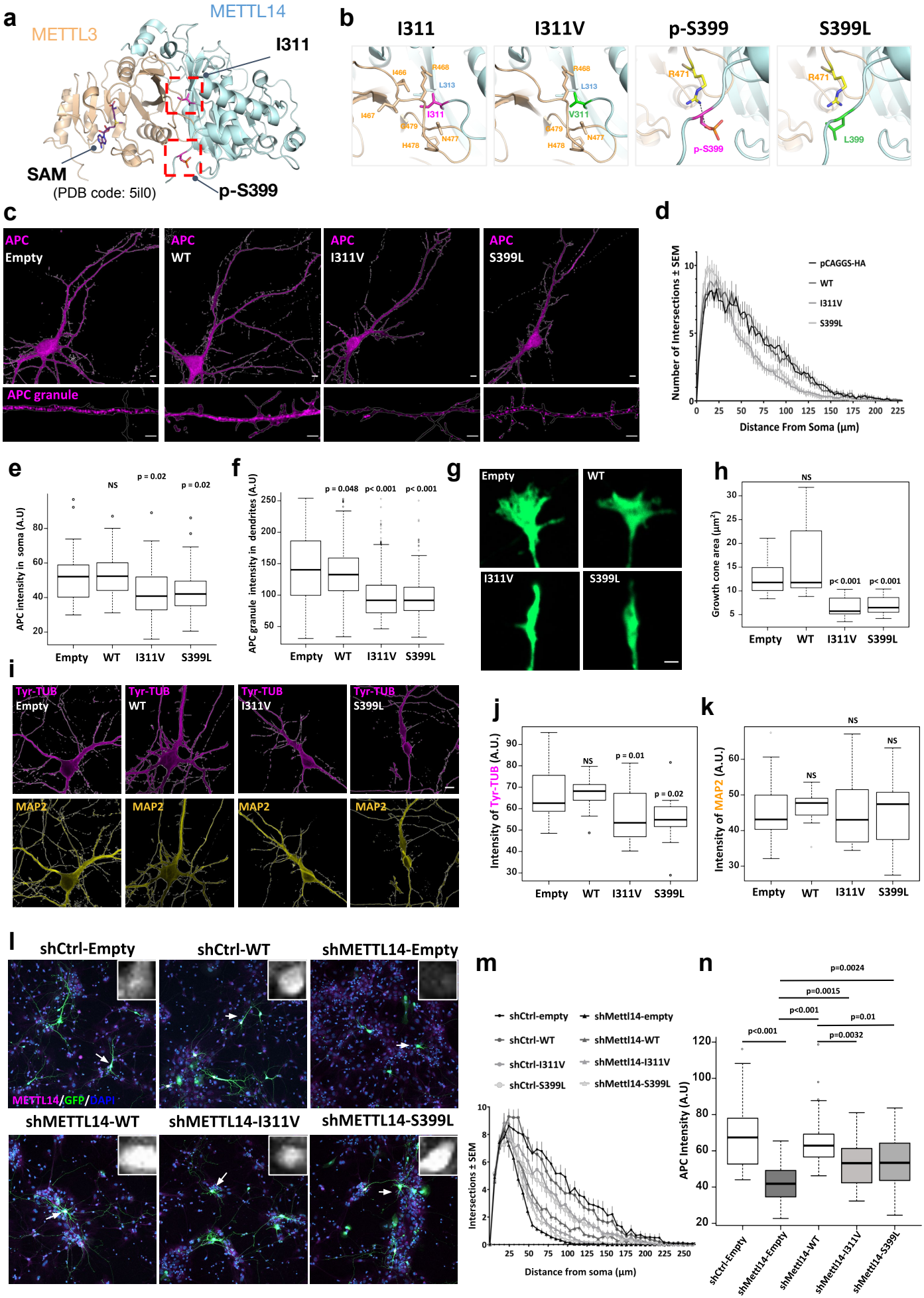
a
METTL3
METTL14
I311
SAM
(PDB code: 5il0)
p-S399
b
I311
I311V
p-S399
S399L
I466
R468
L313
I467
I311
G479
H478
N477
V311
R471
p-S399
L399
c
APC
Empty
WT
I311V
S399L
APC granule
d
Number of Intersections ± SEM
pCAGGS-HA
WT
I311V
S399L
Distance From Soma (µm)
e
APC intensity in soma (A.U)
NS
p = 0.02
p = 0.02
Empty
WT
I311V
S399L
f
APC granule intensity in dendrites (A.U)
p = 0.048
p< 0.001
p< 0.001
g
Empty
WT
I311V
S399L
h
Growth cone area (µm²)
NS
p< 0.001
p< 0.001
i
Tyr-TUB
MAP2
j
Intensity of Tyr-TUB (A.U.)
NS
p = 0.01
p = 0.02
k
Intensity of MAP2 (A.U.)
NS
l
shCtrl-Empty
shCtrl-WT
shMETTL14-Empty
METTL14/GFP/DAPI
shMETTL14-WT
shMETTL14-I311V
shMETTL14-S399L
m
shCtrl-empty
shCtrl-WT
shCtrl-I311V
shCtrl-S399L
shMettl14-empty
shMettl14-WT
shMettl14-I311V
shMettl14-S399L
Intersections ± SEM
Distance from soma (µm)
n
APC Intensity (A.U)
p<0.001
p<0.001
p=0.0015
p=0.0024
p=0.01
p=0.0032
shCtrl-Empty
shMettl14-Empty
shMettl14-WT
shMettl14-I311V
shMettl14-S399L

Figure 7